2

Electrodynamical Analysis of Open Lossy Metamaterial Waveguide and Scattering Structures

L. Nickelson, S. Asmontas, T. Gric, J. Bucinskas and A. Bubnelis
State Research Institute Center for Physical Sciences and Technology, Vilnius, Lithuania

1. Introduction

Large stream of articles devoted to the study of metamaterial waveguide and metamaterial scattering (reflecting) structures points that there is a need for development devices possessing unique characteristics, as multifunctionality, reconfigurability, certain frequency bandwidth, ability to operate at high-powers and high-radiation conditions. The importance of diffraction problems for scattering structures is based on their great practical utility for many applications, such as reflector antennas, the analysis of structures in open space, electromagnetic (EM) defence of structures, the scattering modeling for remote sensing purposes, high frequency telecommunications, computer network, invisibility cloaks technology and radar systems (Li et.al., 2011; Zhou et.al.; 2011, Zhu et al., 2010; Mirza et al., 2009; Abdalla & Hu, 2009; Engheta & Ziolkowski, 2005).

The technological potential of metamaterials for developing novel devices offers a very promising alternative that could potentially overcome the limitations of current technology. The metamaterial waveguide and scattering structures can operate as different devices that possess different specific qualities as well. In order to create a new microwave device it is necessary to know the main electrodynamical characteristics of metamaterial structures on the basis of which the device is supposed to be created.

Here are presented electrical field distributions and dispersion characteristics of open metamaterial waveguides in subsections 1-3 and numerical analysis of the scattered and absorbed microwave powers of the layered metamaterial cylinders in the subsection 4.

2. Analyses of electrical field and dispersion characteristics of square metamaterial lossy waveguides by the SIE method

Here the open (without conductor screen) square metamaterial waveguides with sizes $5x5\ mm^2$ and $4x4\ mm^2$ are investigated by our algorithms that were created on the base of the Singular Integral equations' (SIE) method (Nickelson & Sugurov, 2005; Nickelson et al., InTech2011). Due to the fact that metamaterial is a substance with losses we have determined the complex roots of the dispersion equation by using of the Muller method in our researches (Nickelson et al., InTech2011).

Our computer programmes are written in MATLAB. They let us to investigate open absorptive waveguides with different shapes of cross-section (Gric & Nickelson, 2011). We have used the values of the complex relative permittivity ε_{met} and the complex relative permeability μ_{met} of metamaterial from (Penciu et al, 2006) in suctions 1 and 2.

2.1 Numerical investigations of square 5x5 mm^2 metamaterial waveguide

The dispersion characteristics and the 3D electric field distributions are presented here (Figs 1.1–1.3). The characteristics are shown in Fig. 2.1 (Gric et al., 2010). The main wave (mode) is denoted with black points; the first higher mode is denoted with circles. The values of ε_{met} and μ_{met} are different at every frequency. The real part of the permittivity is always negative at the all frequency range 75-115 GHz. The imaginary part of the permittivity is negative approximately when $90 \leq f \leq 100$ GHz. The real part of the permeability is negative when $100 \leq f \leq 105$ GHz. The imaginary part of the permeability is always equal to zero or a positive number at the all mentioned frequency range. In the Fig. 2.1 are presented dependencies of the complex propagation constant h = h′- i h″ on the frequency.

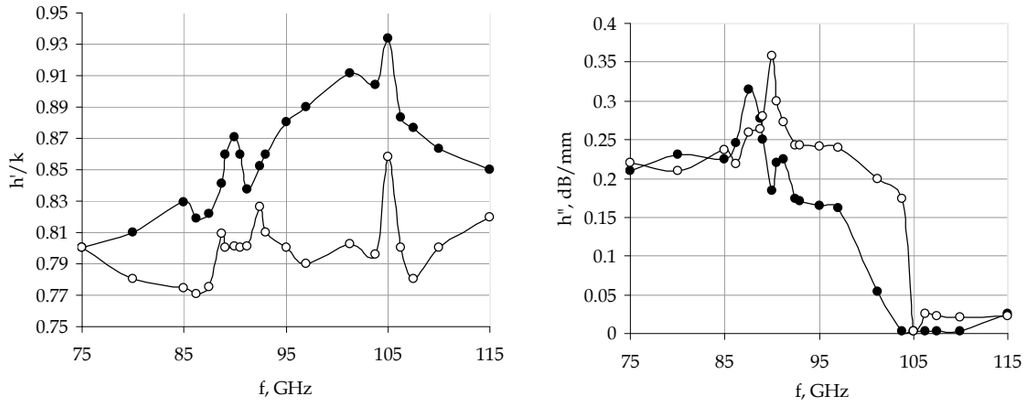

Fig. 2.1. Dispersion characteristics of square 5x5 mm² metamaterial waveguide
(a) – the dependence of the normalized propagation constant, (b) – the dependence of the attenuation constant on frequencies.

In Fig. 2.1(a) we see that dependencies of the normalized propagation constant h'/k on the frequency, where h'=2 π/λ and λ is the wavelength of microwave in the metamaterial waveguide, k=2 π f/c, k is the wavenumber in vacuum, f is an operating frequency, c is the speed of light in vacuum. The curves of the main mode and the first higher mode are not smooth. The magnitudes h′/k <1 for both modes (Fig. 2.1(a)). It means that the main and the first higher modes are the fast waveguide waves. In Fig. 2.1(b) are shown dependencies of the waveguide attenuation constant (losses) h″ on the frequency. We see that the values of the main and higher mode losses are commensurate and the losses are not higher in the frequency range. The loss maximums of the main mode and the first higher mode are slightly shifted. The maximum of main mode losses is 0.32 dB/mm at f = 87.5 GHz and the wavelength of this mode is equal to 4.2 mm. The maximum of the first higher mode is 0.36 dB/mm at f = 90 GHz and the wavelength of this mode is equal to 4 mm (Fig. 2.1). It is important to remark that the losses of the main mode are very low at the frequency range

from 105 GHz till 115 GHz. This feature could be used in practice for creation of feeder lines and specific devices that require low distortions in the signal transmission.

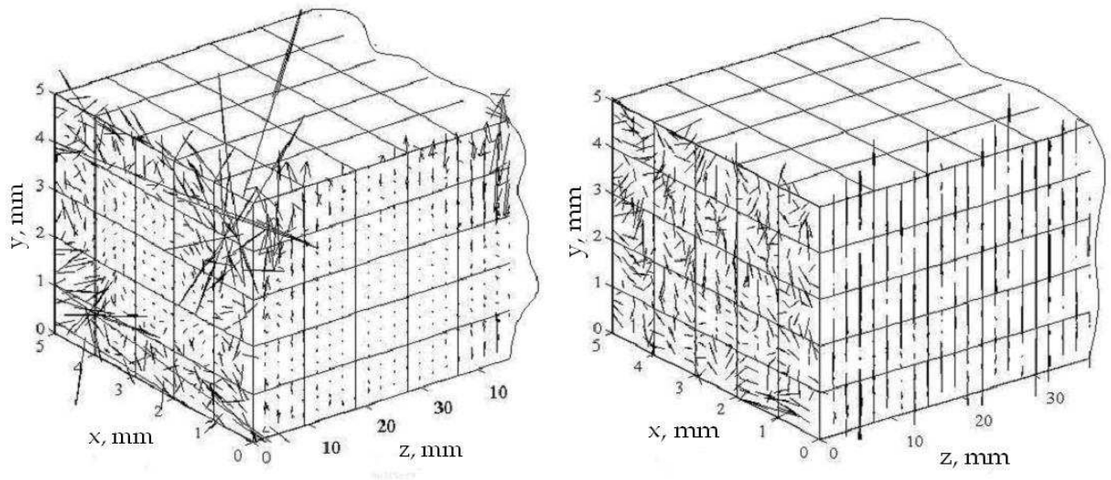

(a) (b)

Fig. 2.2. The 3D electric field distribution of the main mode propagating in the square 5x5 mm² metamaterial waveguide. (a) – f= 95 GHz, (b) – f=110 GHz.

The 3D electric field distributions of the main mode at f = 95 GHz and 110 GHz are shown in Fig. 2.2. The metamaterial has ε_{met} = -23.75-i 18.75 and μ_{met} = 1.75+i 6.25 at f = 95 GHz. The metamaterial has ε_{met} = -10.83-i0.02 and μ_{met} = 0.5 – i 0.01 at f = 110 GHz.

We see that the waveguide losses are large at f = 95 GHz and they are low at f = 110 GHz (Fig. 2.1(b)). We present here the electric field line distribution at these two frequencies in order to compare how the losses influence on the field picture. The calculations of the electric fields in this section were fulfilled at the approximately 10000 points in every cross-section.

The metamaterial is an epsilon-negative media at f = 95 GHz and f = 110 GHz. In Fig. 2.2(a) we see the electric field is very small in the center of the waveguide cross-section. Such distribution can be explained by the large loss at f = 95 GHz and the EM wave does not deeply penetrate into the metamaterial. The refractive index of single negative metamaterial and the transverse propagation constants of waveguide made of the metamaterial are imaginary numbers. For this reason the electric field concentrates near the waveguide border. The tendency of the field to concentrate at the interface of the single negative metamaterial is the important feature of this kind metamaterial.

The behaviour of the EM field components when approaching to the apex of the waveguide cross-section contour (waveguide edge) are an important point of an electrodynamical solution. We would like to note that the condition on the waveguide edge is satisfied in our solutions of considered electrodynamical problems.

Examining the electric field lines near the upper right corner of the square waveguide we would like to note that the electric field lines are directed counter-clockwise on the right side of the corner and the lines are directed clockwise on the left side of the corner. The electric

field lines near the left bottom corner of the square waveguide are distributed in similar way. The lines are directed counter-clockwise on the right side of the corner and they are directed clockwise on the left side of the corner. The electric field lines are diverging of the left bottom corner while the lines are converging to the right upper corner. For this reason, we believe that there is an increased density of electric lines in the upper corner and the weaker density in the bottom corner (Fig. 2.2(a)).

The same effect of no uniformity in the electric field distribution on the waveguide perimeter we can see for the circular waveguide (see below in section 2, Figs 2.2, 2.3).

f = 95 GHz, square waveguide 5x5 mm^2		
E_z [V/m]	E_x [V/m]	E_y [V/m]
$3.765 \cdot 10^{-1}$ - i $6.411 \cdot 10^{-1}$	1.5099-i 2.1941	-0.9943+i 1.9673
H_z [A/m]	H_x [A/m]	H_y [A/m]
$-3.39 \cdot 10^{-2}$ + i $7.51 \cdot 10^{-2}$	$-7 \cdot 10^{-4}$ + i$1.1 \cdot 10^{-3}$	$2.6 \cdot 10^{-3}$ – i $3.9 \cdot 10^{-3}$
f = 110 GHz		
E_z [V/m]	E_x [V/m]	E_y [V/m]
$-1.2766 \cdot 10^{-5}$ – i $1.6592 \cdot 10^{-5}$	0.0134 + i 0.0211	-0.0291 + i 0.0702
H_z [A/m]	H_x [A/m]	H_y [A/m]
$-3.0 \cdot 10^{-3}$ - i $2.9 \cdot 10^{-3}$	$1.3048 \cdot 10^{-4}$ –i $3.0558 \cdot 10^{-4}$	$5.9501\ 10^{-5}$+i $1.0936 \cdot 10^{-4}$

Table 2.1. The EM field components of the main mode at the point with coordinates x = 4 *mm* and y = 4 *mm* when f=95 GHz and f=110 *GHz*

f = 95 GHz, square waveguide 5x5 mm^2		
E_z [V/m]	E_x [V/m]	E_y [V/m]
$3.932 \cdot 10^{-1}$ - i$6.181 \cdot 10^{-1}$	1.3730 - i1.8577	$-9.535 \cdot 10^{-1}$+ i 1.6598
H_z [A/m]	H_x [A/m]	H_y [A/m]
$-3.20 \cdot 10^{-2}$+ i$6.36 \cdot 10^{-2}$	$-8 \cdot 10^{-4}$ + i$1.4 \cdot 10^{-3}$	$2.5 \cdot 10^{-3}$- i$3.4 \cdot 10^{-3}$
f = 110 GHz		
E_z [V/m]	E_x [V/m]	E_y [V/m]
$1.3083 \cdot 10^{-6}$-i$1.2678 \cdot 10^{-5}$	$-4.6 \cdot 10^{-3}$ + i$2.30 \cdot 10^{-2}$	$-2.63 \cdot 10^{-2}$ + i$4.31 \cdot 10^{-2}$
H_z [A/m]	H_x [A/m]	H_y [A/m]
$-1.9 \cdot 10^{-3}$ - i$2.4 \cdot 10^{-3}$	$1.0715 \cdot 10^{-4}$ - i$1.7759 \cdot 10^{-4}$	$-2.7720 \cdot 10^{-5}$+i$1.0632 \cdot 10^{-4}$

Table 2.2. The EM field components of the first higher mode at the point with coordinates x = 4 mm and y = 4 mm when f = 95 GHz and f = 110 GHz

In tables 2.1 and 2.2 we demonstrate the values of complex EM field components of the main mode and the first higher mode at two frequencies. On the base of the table data we can say, that the both modes on these frequencies are hybrid modes.

We do not classified the waveguide modes here in the usual way, e.g. the hybrid magnetic HE_{mn} or the hybrid electric EH_{mn} modes because the kind of mode of strong lossy waveguides may change when we change the frequency [Nickelson et al., 2011; Asmontas et al., 2010].

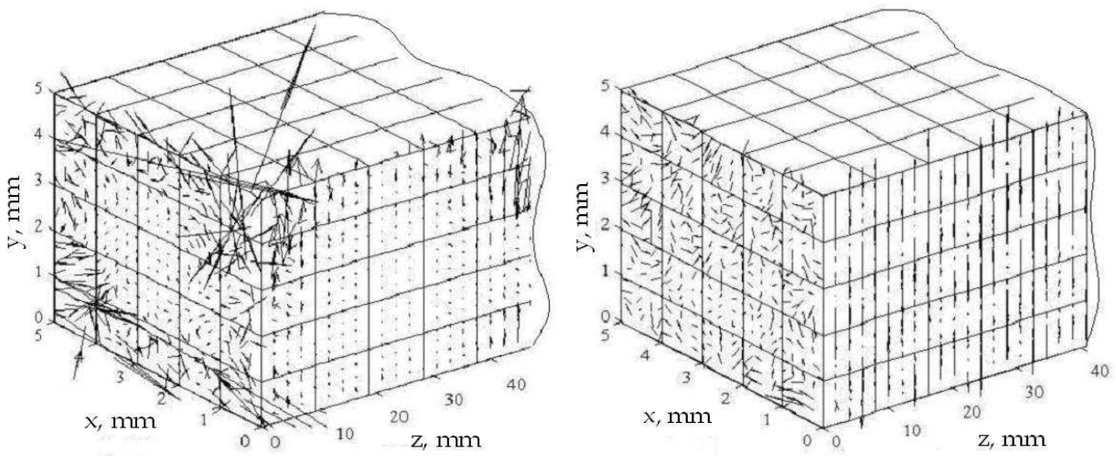

(a) (b)

Fig. 2.3. The 3D electric field distribution of the first higher mode propagating in the square 5x5 mm² metamaterial waveguide. a) – f= 95 GHz, b) – f= 110 GHz.

In Fig. 2.3(a) we see that the electric field at f = 95 GHz for the first higher modes is also concentrated near the metamaterial borders and the strongest field is at two diagonal corners of the cross-section, i.e. at the right upper corner and the left bottom corner. There is a strong asymmetry of the electric field distribution on the perimeter of waveguide. It happened probably by reason that the real and imaginary parts of permittivity are negative and relatively large at this frequency.

In Figs 2.2(b)–2.3 (b) we see that the electric field distributions of the main and first higher modes have a more homogeneous picture in the waveguide cross-section at f = 110 GHz. This happened because the electric field penetrates deeper into the metamaterial at this frequency because the waveguide loss is small at f = 110 GHz (Fig. 2.1(b)). We can also see here some asymmetry of electric field lines on the waveguide cross-section. The projections of the vector electric fields on the waveguide sidewalls are depicted along the waveguide (Figs 2.2-2.3).

2.2 Numerical investigations of square 4x4 mm^2 metamaterial waveguide

The dispersion characteristics of the square metamaterial waveguide are presented in Fig.2.4 (Gric et al., 2010). We used the values of ε_r^m and μ_r^m from (Penciu et al, 2006). In Fig. 2.4(a) the normalized propagation constant h'/k is shown. In Fig. 2.4(a) we see that the magnitude h' is less than the wave number *k* in the frequency range 85-108 GHz. It means that at these frequencies the main and the first higher modes are fast waves. The wavelengths of both modes differ slightly. The losses of both propagating modes in the metamaterial square waveguide change in very complicated way when the frequency increases. Mode losses have several maximums and minimums. We see that the losses of the main mode become a very small at the frequency 103.75 GHz.

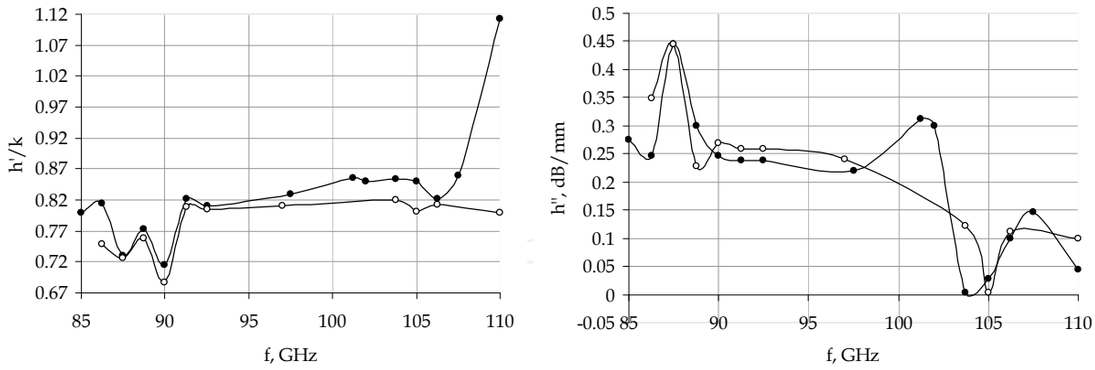

(a) (b)

Fig. 2.4. The dispersion characteristics of the square 4x4 mm² metamaterial waveguide (a) – the dependence of the normalized propagation constant, (b) - the dependence of the attenuation constant on frequencies.

In Fig. 2.5 we see that the electric field is weak inside of square metamaterial waveguide of size 4x4 mm² at f=92.5 GHz. The electric field lines concentrate in the two diagonal waveguide corners in other way in the comparison with the waveguide of size 5x5 mm² at f=95 GHz.

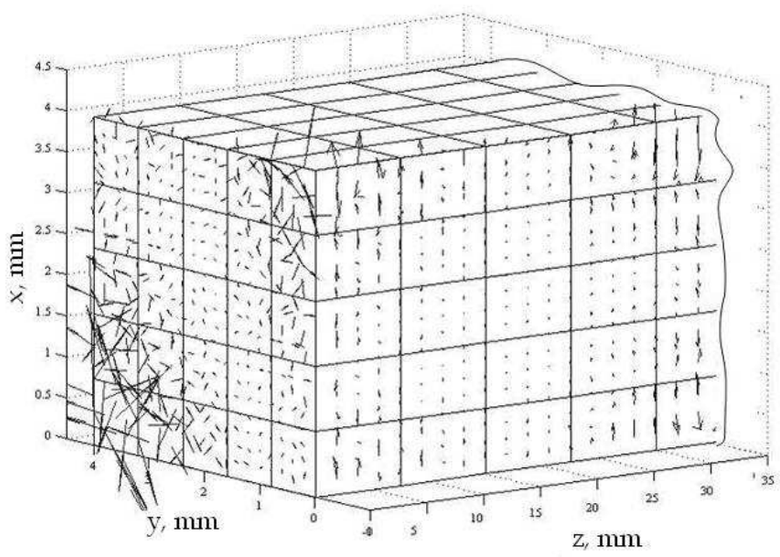

Fig. 2.5. The 3D vector electric field distribution of the main mode propagating in the open square 4x4 mm² metamaterial waveguide at f=92.5 GHz.

The 3D electric field distribution of the main mode at the frequency 92.5 GHz is depicted in Fig. 2.5. The permittivity of the metamaterial at f=92.5 GHz is -35-i2.5 and the permeability is 2.25+i0.25. The metamaterial is a single negative matter. The calculations of the electric fields were fulfilled at the approximately 160 points in every cross-section (Fig 2.5).

3. Investigations of the circular waveguides by the partial area method

Here the open circular metamaterial waveguide is investigated by the partial area method (Nickelson et al., 2008). The presentation of longitudinal components of the electric E_z^m and magnetic H_z^m fields that satisfy to the Maxwell's equations in the metamaterial medium is in the form:

$$E_z^m = A_1 J_m(k_\perp^+ r)\exp(im\varphi), \quad H_z^m = B_1 J_m(k_\perp^+ r)\exp(im\varphi) \tag{3.1}$$

where A_1, B_1 are unknown arbitrary amplitudes, J_m is the Bessel function of the m−th order, $k_\perp^+$ is the transverse propagation constant of the metamaterial medium, r is the radius of the circular metamaterial waveguide, m is the azimuthal index characterizing azimuthal variations of the field, φ is the azimuthal angle. The presentation the electric field E_z^a and the magnetic field H_z^a components that satisfy to Maxwell's equations in air are:

$$E_z^a = A_2 H_m(k_\perp^- r)\cdot\exp(im\varphi), \quad H_z^a = B_2 H_m(k_\perp^- r)\cdot\exp(im\varphi) \tag{3.2}$$

where A_2, B_2 are unknown arbitrary amplitudes, H_m is the Hankel function of the m−th order and the second kind, $k_\perp^-$ is the transverse propagation constant of air medium.

As far as the circular waveguide is researched in the cylindrical coordinate system we have to satisfy the boundary conditions for two components of the electric field (E_φ, E_z) and the magnetic field (H_φ, H_z) on the cylindrical interface metamaterial-air. The condition at infinity also is satisfied. The sign of $k_\perp^-$ changes on the opposite one for the metamaterial hollow-core waveguide, when a hole is surrounded by a metamaterial medium. After substitution of expressions (1) and (2) in the transverse components expressed in terms of the longitudinal components (Kong, 2008) we obtain the expressions of all transverse EM field components. The result of solution is the dispersion equation in the determinant form. We determine complex roots of the dispersion equation by using of the Muller method.

3.1 Investigations of the circular metamaterial waveguide (r=2.5 mm) by the partial area method

We discovered the particularity in the electric field distribution on the cross-section of the open circular metamaterial waveguide at the operating frequency 95 GHz. We find that this waveguide could be used as a narrowband filter at frequencies 102-102.5 GHz.

The circular metamaterial waveguide with r=2.5 mm was researched. The dispersion characteristics and the 3D electric and magnetic field distributions were calculated (see Figs 2.1-2.5). The dispersion characteristics are presented in Fig. 3.1. The main mode is denoted with black points and the first higher mode is denoted with circles.

In Fig. 3.1 (a) we see that the normalized propagation constants of the main and the first higher modes are fairly smooth except only one protrusion at frequencies between 97 GHz and 102 GHz. There is a large peak of the main mode losses at frequency f = 101.25 GHz. At this frequency metamaterial is double negative with $\varepsilon_{r,met}$ = -9.17 -i0.83 and $\mu_{r,met}$ = -0.75. We see that losses of the main mode are very small at the frequency ranges 75-100 GHz and 102.5-115 GHz. While the losses of the first higher mode are significantly higher at this frequency ranges

(Fig. 3.1(b)). Therefore the investigated circular metamaterial waveguide can be used as a filter at the frequencies 100-102.5 GHz and as a one mode lossless waveguide at the frequency ranges 75-100 GHz and 102.5-115 GHz. As we can see the first higher mode is a quickly attenuated wave because it has very large losses in all frequency range.

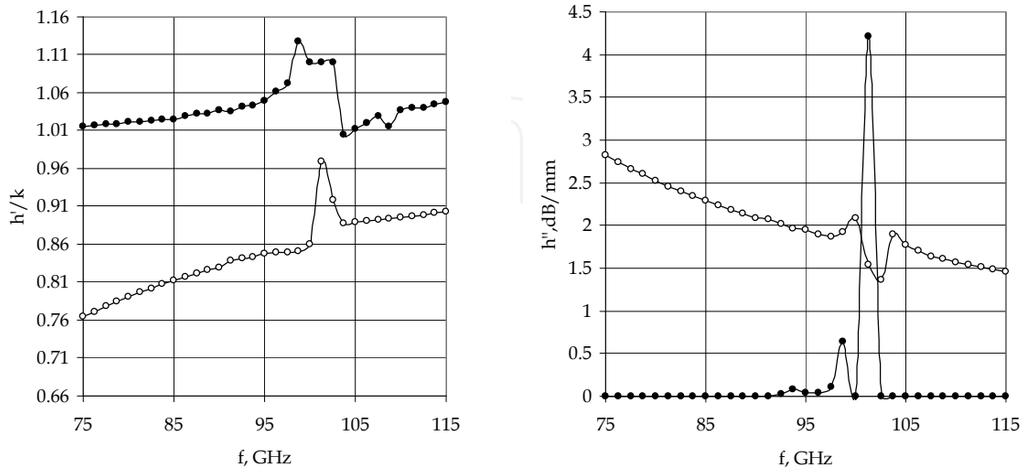

(a) (b)

Fig. 3.1. The dispersion characteristics of the circular metamaterial waveguide with r=2.5 mm (a) – the dependence of the normalized propagation constant, (b) – the dependence of the attenuation constant on frequencies.

The 3D electric field distributions of the main mode were calculated at frequencies 95 GHz and 110 GHz (Fig. 3.2 and 3.3) as well as the first higher mode at the same frequencies (Fig. 3.4 and 3.5). The electric field inside the circular metamaterial waveguide is much smaller than outside of waveguide for this reason we have increased the electric field strength lines inside of the waveguide in order to see them (Figs 3.2(b) – 3.5(b)).

Because the metamaterial has more losses at 95 GHz than at 110 GHz, so the electric field inside of waveguide is weaker at 95 GHz (see tables 3.1, 3.2) compare to the inner electric field at 110 GHz. On this reason we increased the electric field strength lines at 95 GHz in the 143 times and at 110 GHz in the 14 time. The calculations of the electric fields were fulfilled at the approximately 10000 points in every cross-section.

f = 95 *GHz*, waveguide diameter 5mm		
E_z [V/m]	E_x [V/m]	E_y [V/m]
$-2.5897 \cdot 10^{-5} + i2.7266 \cdot 10^{-4}$	$-2.8425 \cdot 10^{-5} + i1.9342 \cdot 10^{-5}$	$4.5991 \cdot 10^{-6} - i3.3487 \cdot 10^{-5}$
H_z [A/m]	H_x [A/m]	H_y [A/m]
$2.5111 \cdot 10^{-7} - i2.0158 \cdot 10^{-7}$	$-2.3843 \cdot 10^{-8} - i2.8570 \cdot 10^{-8}$	$2.5496 \cdot 10^{-6} + i1.8364 \cdot 10^{-7}$
f = 110 *GHz*		
E_z [V/m]	E_x [V/m]	E_y [V/m]
$0.0067 + i0.0067$	$-0.0027 + i0.0027$	$-7.8928 \cdot 10^{-4} - i7.8928 \cdot 10^{-4}$
H_z [A/m]	H_x [A/m]	H_y [A/m]
$3.1409 \cdot 10^{-12} - i1.1109 \cdot 10^{-5}$	$-3.3354 \cdot 10^{-6} - i3.3354 \cdot 10^{-6}$	$7.1930 \cdot 10^{-5} - i7.1930 \cdot 10^{-5}$

Table 3.1. The electromagnetic field components of the main mode at the point with coordinates r = 2 mm, φ = 45° when f = 95 and f = 110 GHz

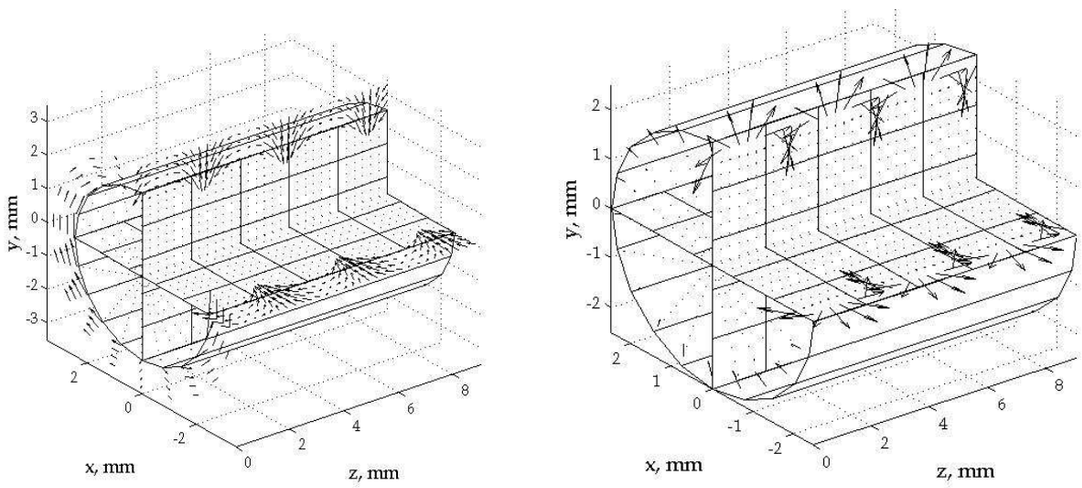

(a) (b)

Fig. 3.2. The 3D electric field distributions of the main mode of circular metamaterial waveguide with r=2.5 mm at f = 95 GHz. (a) – the electric field strength lines outside the waveguide (b) – the 143 times were increased electric field strength lines inside the waveguide.

In In Figs 3.2–3.5 we see that the electric field is irregular on the waveguide perimeter of the cross-section while the cross-section of the waveguide is a circle. We see that and the most part of the electric field localizes on the border and outside of the waveguide. The electric field is strongest outside the waveguide when φ is 0 or π radians. The electric field has the minimum values and the electric field lines are directed clockwise or counter-clockwise to the right and left of the points with φ equal to π/2 or 3π/2 radians (Figs 3.2(a)–3.5(a)). We see that at the points when the electric field outside of the metamaterial waveguide has the maximum value the field inside of the waveguide is minimal. In Figs 3.2(b)–3.5(b) we see that the maximum electric field inside the metamaterial waveguide is when φ is equal to π/2 or 3π/2 radians. The length of the circular waveguide in z-direction (the Figs 3.2– 3.5) is three times longer than wavelength of microwave in the waveguide in our calculations.

f = 95 *GHz,* waveguide diameter 5 mm		
E_z [V/m]	E_x [V/m]	E_y [V/m]
$1.6760 \cdot 10^{-4}$ -i$3.3526 \cdot 10^{-4}$	$3.5399 \cdot 10^{-5}$-i$1.2553 \cdot 10^{-5}$	$-2.7112 \cdot 10^{-5}$-i$1.2042 \cdot 10^{-6}$
H_z	H_x	H_y
$-1.8851 \cdot 10^{-7}$-i$1.9128 \cdot 10^{-7}$	$4.6704 \cdot 10^{-8}$+i$8.1377 \cdot 10^{-8}$	$-3.1731 \cdot 10^{-6}$-i$1.4861 \cdot 10^{-6}$
f = 110 *GHz*		
E_z [V/m]	E_x [V/m]	E_y [V/m]
$-5.3 \cdot 10^{-3}$ -i$1.22 \cdot 10^{-2}$	$4.1 \cdot 10^{-3}$ -i$2.1 \cdot 10^{-3}$	$-3.2013 \cdot 10^{-4}$ +i$9.6358 \cdot 10^{-4}$
H_z	H_x	H_y
$-1.0713 \cdot 10^{-5}$+i$9.0740 \cdot 10^{-7}$	$7.1766 \cdot 10^{-6}$+i9.3919	$-1.3582 \cdot 10^{-4}$+i$5.6938 \cdot 10^{-5}$

Table 3.2. The EM components of the first higher mode with coordinates at the point with coordinates r = 2 mm , φ = 45° when f=95 and f=110 GHz

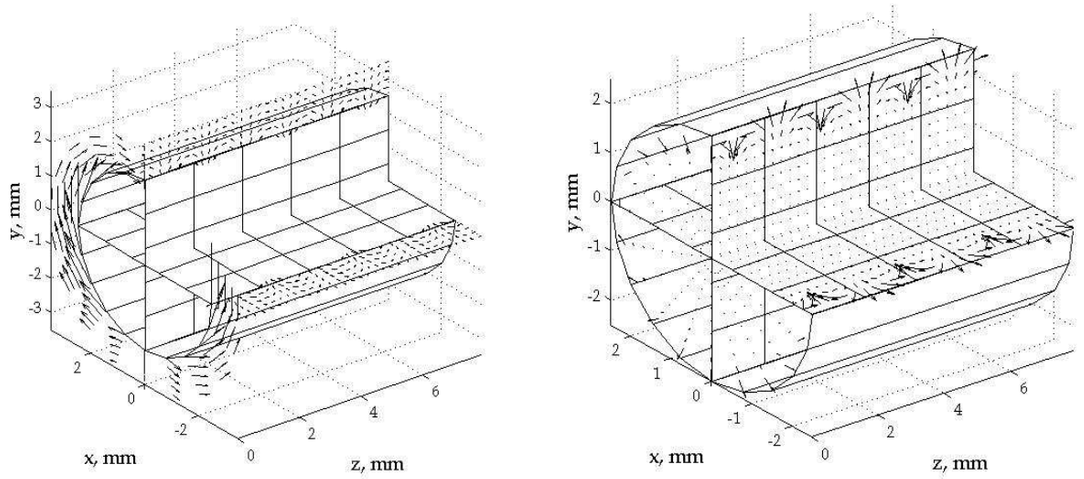

(a) (b)

Fig. 3.3. The 3D electric field distributions of the main of circular metamaterial waveguide with r=2.5 mm at f = 110 GHz. (a) – the electric field strength lines outside the waveguide (b) – the 14 times were increased electric field strength lines inside the waveguide

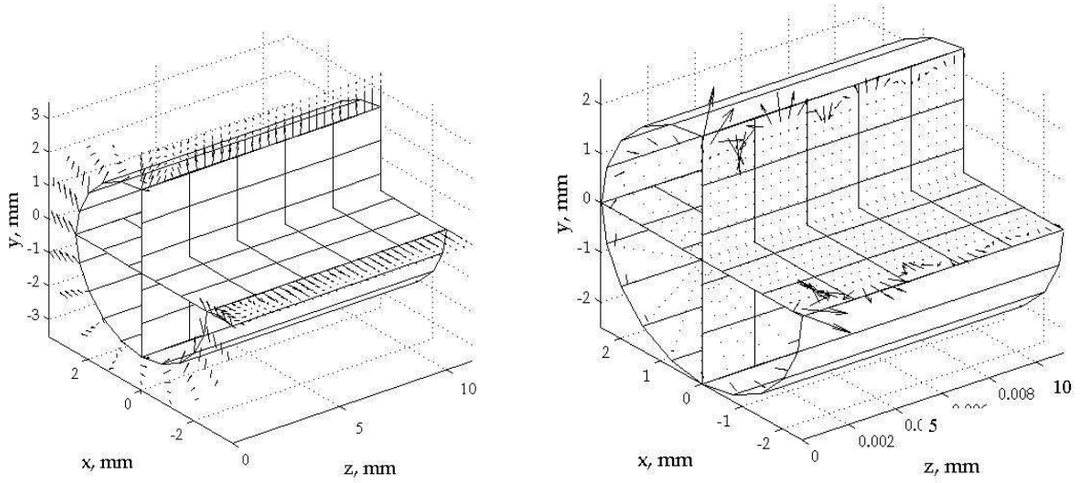

(a) (b)

Fig. 3.4. The 3D electric field distributions of the first higher mode of circular metamaterial waveguide with r=2.5 mm at f = 95 GHz (a) – the electric field strength lines outside the waveguide (b) – the 143 times were increased electric field strength lines inside the waveguide

We can see that the electric field along the waveguide changes periodically (Figs 3.2–3.5). Comparing Figs 3.2(a) and 3.3(a) we see that the main mode' electrical field at 110 GHz is large and have a little different distribution in longitudinal direction in comparison with the electrical field at 95 GHz. Since the waveguide losses of the main mode at frequencies 95

GHz and 110 GHz are small (please, compare with losses of square waveguide (Fig.2.1)), for this reason the electric field amplitudes vary slightly in the longitudinal direction. Comparing Figs 3.4 and 3.5 we see that the larger is the electrical field outside of the waveguide at the point with a certain angle φ the smaller is the electrical field inside of waveguide at the point with the same φ. The last statement is true for all the investigated cases. The electric field amplitude of the first higher mode became smaller in longitudinal direction with increasing of coordinate z (Figs 3.4(b) and 3.5(b)). We observe in this case, the fast wave attenuation. It happened because the losses of the first higher mode at 95 GHz and 110 GHz are enough large in comparison with the main mode (Fig. 3.1(b)).

The electrical field inside of the waveguide is very small at all frequencies. However the observable electric field strength lines appear at the waveguide boundary.

We would like to note that the boundary conditions on the border of waveguide are satisfied, i.e. the tangential components of electric and magnetic fields are equal on the interface air-metamaterial. For this reason when the electric field lines has a tangential character outside the waveguide (Figs 3.2(a), 3.3(a)) the same character of tangential components has to be on the interface of the metamaterial side. The direction of electric field lines changes with removing deeper in the metamaterial from the interface.

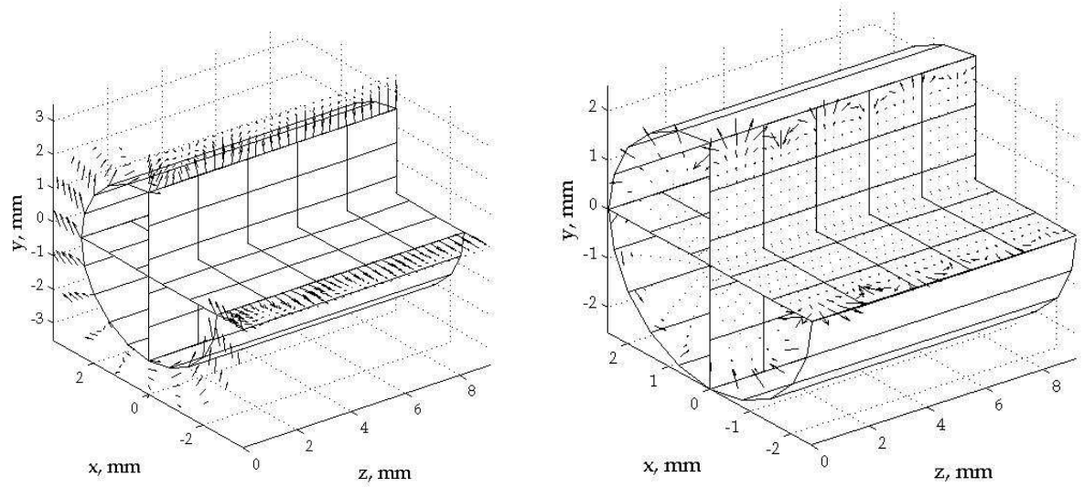

(a) (b)

Fig. 3.5. The 3D electric field distributions of the first higher mode of circular metamaterial waveguide with r=2.5 mm at f = 110 GHz (a) – the electric field strength lines inside the waveguide (b) – the 14 times were increased electric field strength lines outside the waveguide.

Comparing dispersion characteristics of square and circular waveguides (Figs 2.1 and 3.1) we see that they are different due to the boundary conditions, which have a strong influence on the dispersion characteristics in our frequency range. As an additional example, the dispersion characteristic ($2\pi f \cdot SQRT(\varepsilon_{r,met}\ \mu_{r,met})$ of plane EM wave propagating in the same metamaterial only when the one has the infinite dimensions is strongly different in comparison with the waveguide dispersion characteristics. The relatively small losses of the EM wave in the infinite metamaterial are only at the frequencies between 102.5 GHz and 105 GHz.

We would like to draw attention to the fact that the feature of the irregular distribution of electric field lines in the cross-section of square and circular metamaterial waveguides at 95 GHz is very similar.

3.2 Investigations of the circular metamaterial waveguide (r = 2 mm) by the partial area method

3.2.1 The metamaterial rod waveguide

We have investigated circular metamaterial waveguides by our algorithm that was created using the partial area method (Nickelson et al., 2008).

In Fig. 3.6 the dispersion characteristics of the metamaterial waveguide are presented. In Fig. 3.6 (a) the normalized propagation constant h'/k of the main mode and the first higher mode is shown. The main mode is denoted with black points and the first higher mode is denoted with circles.

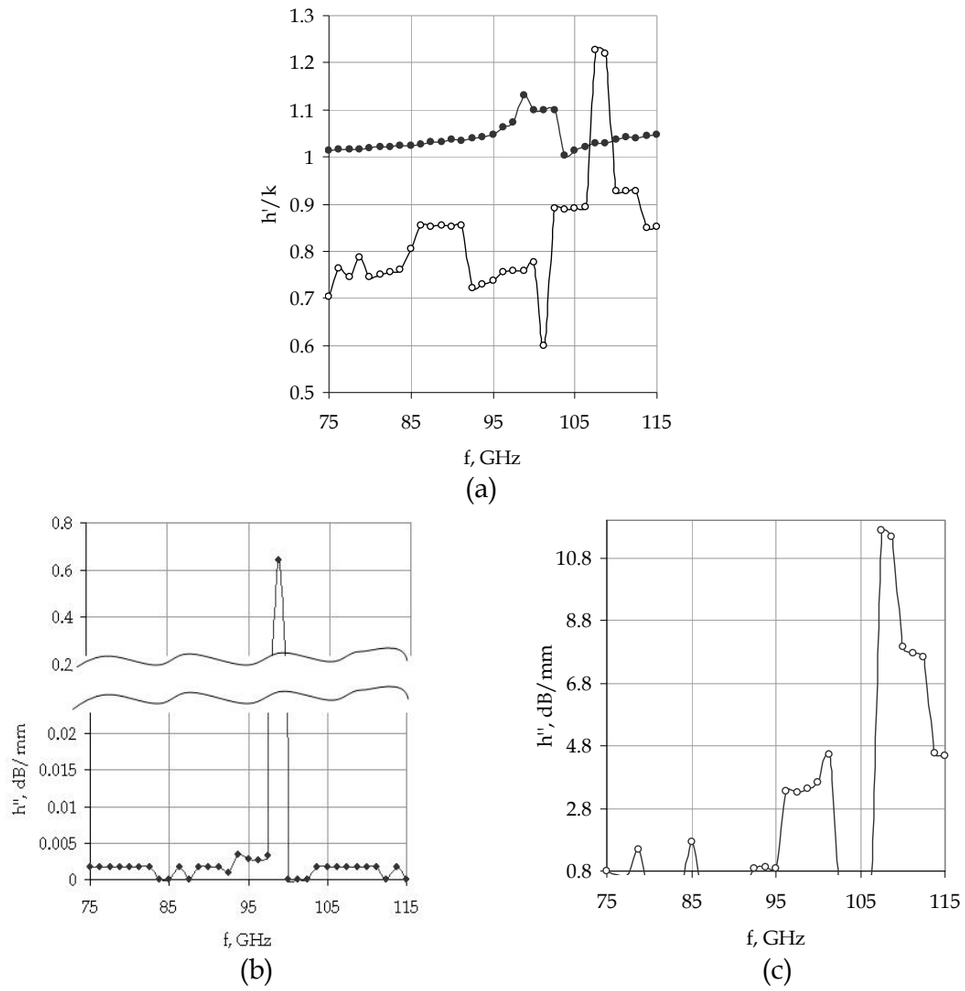

Fig. 3.6. The dispersion characteristics of the circular metamaterial waveguide with r=2 mm (a) – the dependence of the normalized propagation constant, (b), (c) – the dependence of the attenuation constant on frequencies.

In Fig. 3.6 (b) losses of the main mode are shown. In Fig. 3.6 (c) losses of the first higher mode are presented. We show the losses of the modes in the different scales because the losses are not commensurate. We see (Fig. 3.6 (a)) that the main mode is a slow mode and the first higher mode can be a slow mode or a fast mode dependent on the frequency range.

There are two frequency ranges 75-97.5 GHz and 100-115 GHz when losses of the main mode are extremely small. On the other side there are frequency ranges, for example f=95 - 101.25 GHz and f=107.5-115GHz when losses of the first higher mode are large.

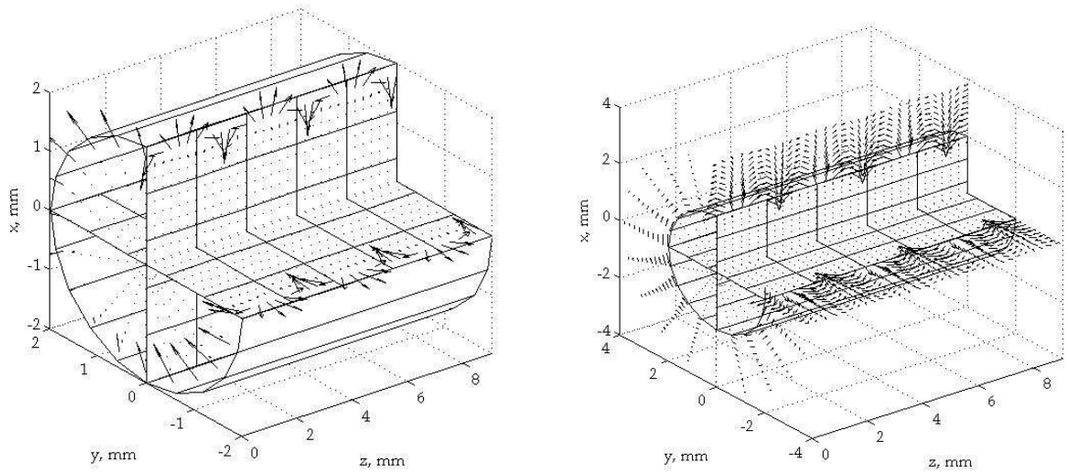

(a) (b)

Fig. 3.7. The 3D vector electric field distributions of the main mode of circular metamaterial waveguide with r=2mm (a) – inside; (b) – inside and outside it.

We have calculated the 3D vector electric field distributions of the main mode propagating in the open circular metamaterial waveguide. The calculation was fulfilled inside and outside the waveguide in 1500 points. The electric field distributions were calculated at frequency f=95 GHz. At this frequency the metamaterial is single-negative. At this frequency $\varepsilon_{r,met}$ = -23.75- i18.75 and $\mu_{r,met}$ = 1.75+ i1.625.

In Fig. 3.7(a) an enlarged picture of the electric field lines inside the metamaterial waveguide is shown. We see that the strongest electric field is in the thin surface layer which is located at the interface metamaterial-air. In Fig. 3.7(b) the electric field lines inside and outside of the metamaterial waveguide are shown. In Fig. 3.7(b) we see that the electric field inside the waveguide is significantly weaker than outside it. We also clearly see that the electric field distributions are periodically repeated in the longitudinal direction.

3.2.2 The metamaterial hollow-core waveguide

The dispersion characteristics of the metamaterial hollow-core waveguide with the radius of the hole (in the metamaterial medium) equal to 2 mm are presented in Fig. 3.8.

In Fig. 3.8 (a) dispersion characteristics of the main and the first higher modes are presented. Both modes are the fast ones. Their electromagnetic energy concentrates in the hollow-core

air area. There are the frequency ranges where modes propagate with very small losses. We can see that losses of the main mode in the frequency range 75-90 GHz and 104-115 are very low and they can be large in the frequency range 91.25-103.75 GHz. The first high mode' losses change abruptly. The losses can be very low at some frequencies approximately 75- 87 GHz, 106 and 111 GHz.

Losses of the first high mode are low and this mode can easily propagate and it can modulate the amplitude of the main mode in devices that were created on the base of the metamaterial waveguide with r=2 mm. There is also good possibility to create a devise on the base of the first high mode in the range f=95-105 GHz.

We have calculated the 3D vector electric field distributions of the main mode propagating in the hollow-core metamaterial waveguide. The electric field distributions were calculated at frequency f = 95 GHz. The calculations of the electric fields were fulfilled at the approximately 10000 points in every cross-section.

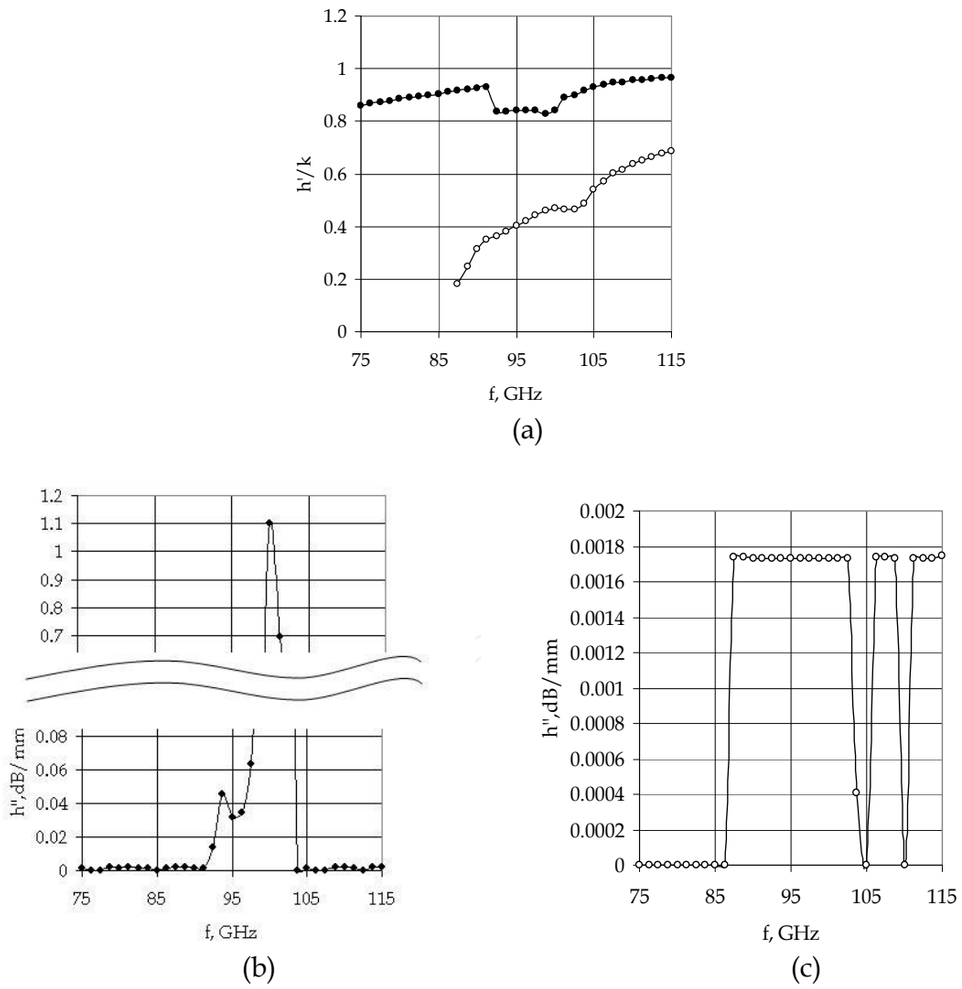

Fig. 3.8. The dispersion characteristics of the hollow-core metamaterial waveguide with r=2 mm (a) – the dependence of the normalized propagation constant, (b)& (c) – the dependence of the attenuation constant on frequencies.

In Fig. 3.9 we see that the electric field inside the air hole is significantly weaker than outside in the metamaterial media. We also clearly see that the electric field distributions are periodically repeated in the longitudinal direction. As the waveguide losses exist only in the metamaterial and the most part of EM energy propagates into air hole then we see no decrease in the amplitude of the electric field with a change in coordinate z (please, compare with Figs 3.4(b), 3.5(b)).

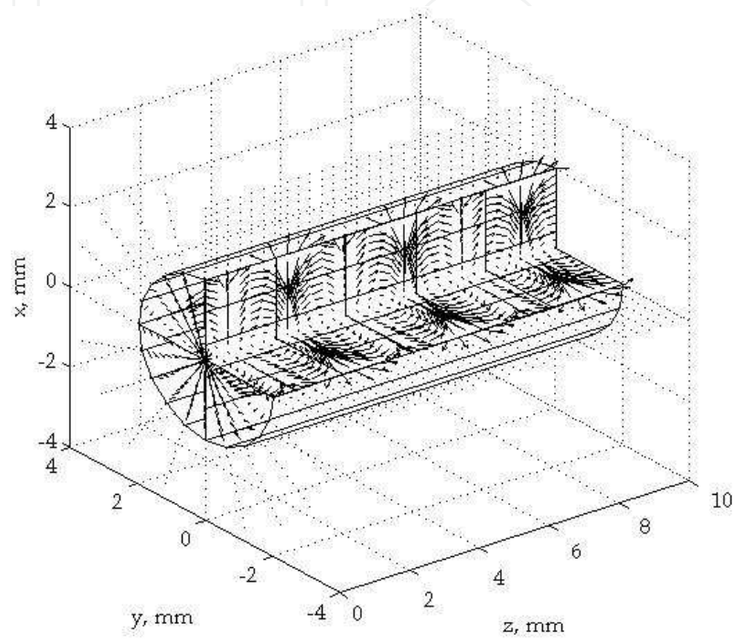

Fig. 3.9. The 3D vector electric field distribution of the main mode of the hollow-core metamaterial waveguide with r=2 mm at frequency 95 GHz.

4. Conclusions on sections 2&3

1. The open lossy metamaterial waveguides with different shapes of the cross-section were investigated by using of our computer programs that have written in MATLAB language. The computer codes were based on the method of singular integral equations and the partial area method.
2. We have calculated the dispersion characteristics (the propagation and attenuation constants) at the frequency range 75-115 GHz as well as the 2D and 3D electromagnetic field distributions. We took the electromagnetic parameters of metamaterial close to practice. Our computer algorithms can be useful working out microwave devices on the base of waveguides made of strong lossy materials.
3. We discovered the special feature of the open lossy metamaterial waveguides. Propagation and attenuation constants depend on the waveguide sizes in an unpredictable complex manner. E.g., the circular metamaterial waveguide with r=2.5 mm (Fig. 3.1) and r=2 mm (Fig. 3.6).
4. The microwave signals propagating on the open metamaterial waveguides (r=2.5 mm) are absorbed at the narrow 2.5 GHz frequency range. This waveguide can be used as a band-stop filter at f_1=100-102.5 GHz when the losses in the passing frequencies 75-100, 102.5-115 GHz are 100 times less than losses at f_1.

5. Investigated EM fields of square and circular waveguides have irregular distributions on the waveguide perimeter. Investigated EM field lines for the main and first higher modes of the squire waveguides are concentrated near the metamaterial borders and the strongest field is at two diagonal corners of the cross-section. The electric field lines are diverging of the one corner while the lines are converging at the other corner.

5. Dispersion characteristic analysis of circular anisotropic metamaterial waveguide with the effective metamaterial permittivity and permeability near to zero

5.1 Introduction

In the past several years many specialist focused on the experimental and theoretical investigations of the zero-refractive index (or zero-index) metamaterials. These metamaterials attracted researches due to their unconventional constitutive parameters and anomalous effects to work out novel electromagnetic devices. Zero- index metamaterial may have the epsilon-near-zero (ENZ) or mu-near-zero (MNZ) properties simultaneously or in turn, one after another at different frequencies.

Zero-index metamaterials are dispersive (electromagnetic parameters dependence on a frequency) media. The constitutive parameters of anisotropic dispersive metamaterials can be described by expressions that involve the plasma frequencies. The metamaterial on frequencies near to plasma resonances is called a plasmonic metamaterial.

Zero-index metamaterials are used in different devices as a transformer to achieve the perfect impedance match between two waveguides with a negligible reflection or to improve the transmission through a waveguide bend as well as for the matching of waveguide structure impedance with the free space impedance (when the metamaterial epsilon and mu are simultaneously very close to zero). Plasmonic metamaterial provides manipulating of the antenna phase fronts and enhancing the antenna radiation directivity. In a Zero-index metamaterial waveguide can be observed a super-tunneling effect. ENZ metamaterials may allow reducing of waveguide sizes and can be used as a frequency selective surface (Bai et al., 2010; Ko&Lee, 2010; Lopez-Garcia et al., 2011; Luo et al., 2011; Wang & Huang, 2010; Oraizi et al. 2009; Zhou et al., 2009, Liu et al., 2008).

5.2 Analysis and simulation of phase constant dependencies

Here we presented the phase constant (real part of the waveguide longitudinal propagation constant) of propagating modes on the circular anisotropic metamaterial waveguide when the metamaterial permittivity and permeability may take values close to zero at certain frequencies. Further we call a plasmonic waveguide.

The solution of Maxwell's equations for the circular anisotropic metamaterial waveguide was carried out by the partial area method (Nickelson et al., 2009). The computer program for the dispersion characteristic calculations has created in MATLAB language. Computer program allows take into account a very large material attenuation (Nickelson et al., 2011; Asmontas et al., 2010). In this section constitutive parameters of the uniaxial electrically and magnetically anisotropic metamaterial were taken from the article (Liu et al., 2007). In the mentioned article was considered an anisotropic dispersive lossless metamaterial slab. For

this reason there were given only the real parts of the permittivity $\varepsilon_{r,ij} = (\varepsilon_{xx}, \varepsilon_{xx}, \varepsilon_{zz})$ and permeability $\mu_{r,ij} = (\mu_{xx}, \mu_{xx}, \mu_{zz})$ tensor components.

The tensor components of the relative permittivity and the relative permeability are described by following formulae (Liu et al., 2007):

$$\varepsilon_{xx}=1-\omega^2_{epxx}/\omega^2, \quad \varepsilon_{zz}=1-\omega^2_{epzz}/\omega^2, \tag{5.1}$$

$$\mu_{xx}=1-\omega^2_{mpxx}/\omega^2, \quad \mu_{zz}=1-\omega^2_{mpzz}/\omega^2, \tag{5.2}$$

here $\omega=2\pi f$ is the angular frequency of microwaves, f is the operating frequency. The electric plasma frequencies of metamaterial are $\omega_{epxx}= 2\pi f_{epxx}$, $f_{epxx}=(12)^{1/2}$ GHz, $\omega_{epzz}=2\pi f_{epzz}$, f_{epzz}=2.5 GHz. The magnetic plasma frequencies of metamaterial are $\omega_{mpxx}= 2\pi f_{mpxx}$ GHz, $f_{mpxx} = (6)^{1/2}$ GHz and $\omega_{mpzz}=2\pi f_{mpzz}$ GHz, f_{mpzz}=2 GHz. The values of angular frequencies are taken from (Liu et al., 2007). The magnitudes of tensor components ε_{xx}, ε_{zz}, μ_{xx}, μ_{zz} are real numbers. In Fig. 5.1(a,b) are presented their dependencies on the frequency.

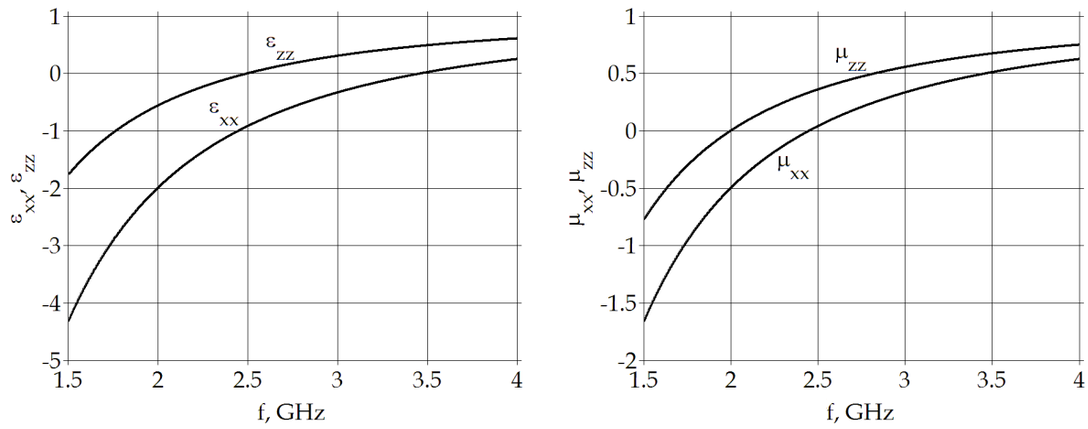

Fig. 5.1. Dependences of the relative (a) permittivity and (b) permeability tensor components of the metamaterial on the frequency.

We see that the permittivity components ε_{xx} and ε_{zz} have negative values from 1.5 to ~3.5 GHz and from 1.5 to ~2.5 GHz, respectively. The permeability components μ_{xx} and μ_{zz} have negative values from 1.5 to~2.5 GHz and from 1.5 to ~2 GHz, respectively. We realize that all tensor components are negative at the frequency range from 1.5 GHz to ~2 GHz. Absolute values of tensor components are less than 1 at the frequency range from ~2.5 GHz to 4 GHz.

The values of tensor components become equal to zero at the operating frequency f equal to the metamaterial electric f_{epxx}=3.46 GHz, f_{epzz}= 2.5 GHz or magnetic f_{mpxx} =2.45 GHz, f_{mpzz}=2 GHz plasma frequencies.

In Figs. 5.2–5.7 are shown dispersion characteristics (phase constants) of open circular waveguide made of the uniaxial electrically and magnetically anisotropic metamaterial. The calculations are performed for the left-handed (extraordinary) circularly polarized microwaves when exp(+imφ), m=0, 1, 2,…is the wave (mode) azimuthal periodicity index, φ is the azimuthal coordinate. We investigated only modes with the index m=1, because it is

known the main mode of open circular dielectric waveguide specify by m=1 and the main mode of a dielectric waveguide is a hybrid mode HE_{11} (Nickelson et al., 2009).

Here is presented the phase constant h‘ (the real part of longitudinal propagation constant) dependencies of plasmonic metamaterial waveguides with radii r equal to 0.1 mm, 1 mm, 3 mm, 5 mm, 7 mm, 10 mm and 15 mm. The phase constant h‘ is equal to $2\pi/\lambda_w$, where λ_w is the wavelength of certain mode. Our aim is to investigate how an increase in the plasmonic waveguide radius affects on the eigenmode numbers, mode cutoff frequencies and a shape of dispersion characteristics.

The analysis of Figs 5.2-5.5 shows that there are three main frequency areas where localize dispersion curves.

A shape all dispersion characteristics Figs 5.2-5.5 are unusual in the comparison with traditional dispersion characteristics of open cylindrical waveguides made of dielectrics, semiconductors or magnetoactive semiconductor plasma (Nickelson et al., 2011; Asmontas et al., 2009; Nickelson et al., 2009). Because the dispersion characteristic branches of analyzed plasmonic waveguides are vertical.

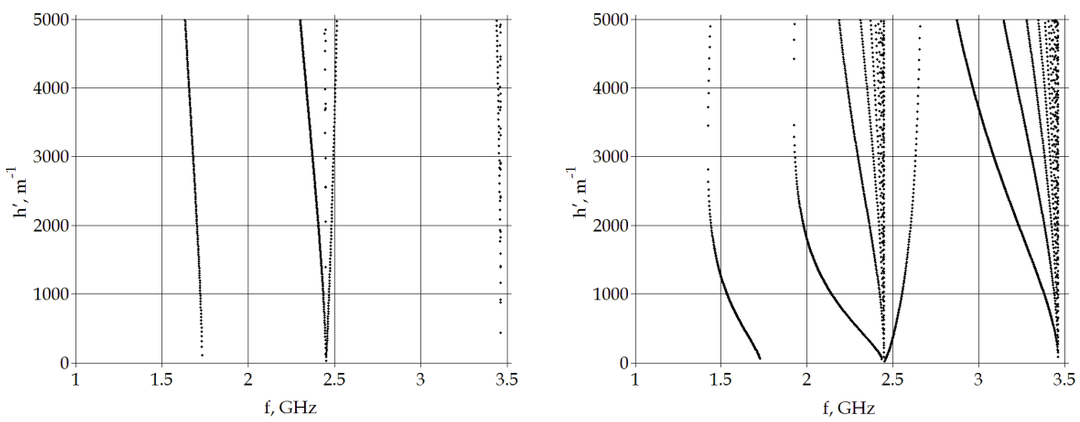

Fig. 5.2. The phase constant dependencies of propagating modes on the anisotropic metamaterial waveguide with (a) r=0.1 mm and (b) r=1 mm.

We see that there is a single mode with the cutoff frequency close to f=1.5 GHz. The cutoff frequency of this mode shifted in the direction of lower frequencies with increasing of the waveguide radius. This first single mode is special one because the mode does not match any of plasma f_{epxx}, f_{epzz}, f_{mpxx}, f_{mpzz} frequencies. We can observe how a shape of the dispersion characteristic changes in the vicinity of the cutoff frequency.

We would like to draw your attention to the fact that the anisotropic metamaterial is described by the negative tensor components ε_{xx}, ε_{zz}, μ_{xx}, μ_{zz} in the frequencies less than 2 GHz (see formulae 5.1 and 5.2). It is mean that the first mode propagates in the waveguide when the metamaterial is double negative (DN). This wave is particularly important because small changes in frequency produce large changes in phase.

We can watch a package of dispersion branches closed to cutoff frequency 2.5 GHz. We see that the left lateral dispersion branch of the package is a special eigenmode, i.e. this one is

separated by a larger distance from other eigenmodes. The vertical branch of the left lateral mode is located at the magnetic plasma f_{mpzz} frequency equal to 2 GHz. We can distinguish also the right lateral dispersion branch of the package. The mode with this dispersion characteristic is also more specific one. i.e. this mode is separated by a larger distance from other modes. The vertical branch of this mode is located about 2.7 GHz and shifted on the higher frequency side with increasing of a radius.

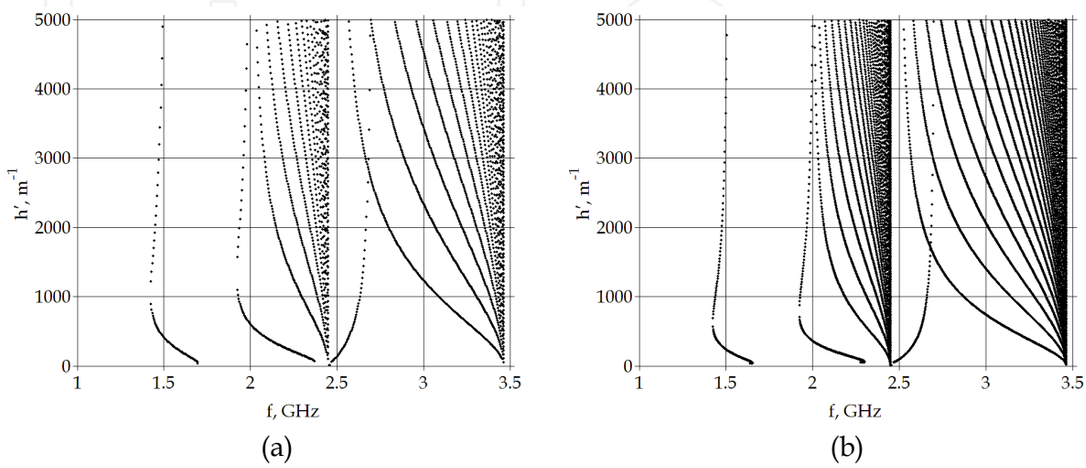

Fig. 5.3. The phase constant dependencies of propagating modes on the anisotropic metamaterial waveguide with (a) r=3 mm and (b) r =5 mm.

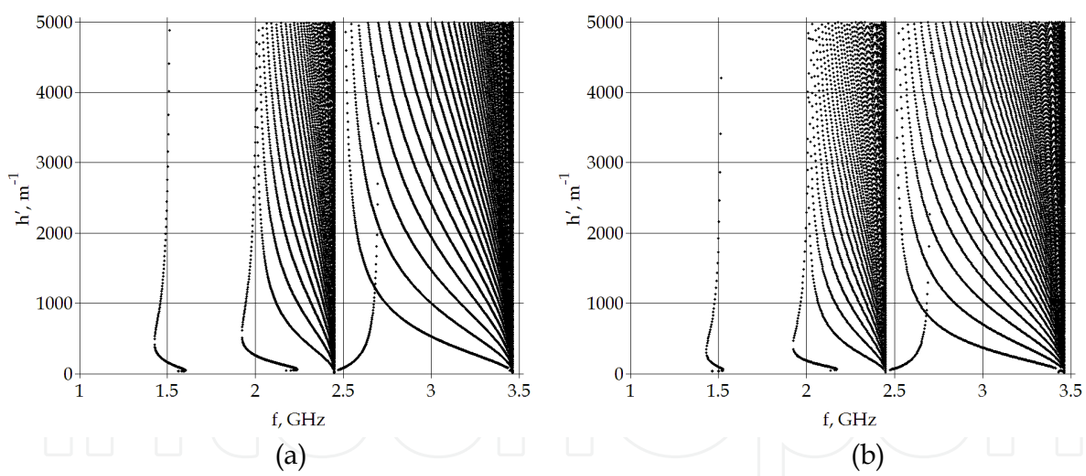

Fig. 5.4. The phase constant dependencies of propagating modes on the anisotropic metamaterial waveguide with (a) r=7 mm and (b) r=10 mm.

A dense bunch of dispersion curves located between the extreme left and right curves that were previously described. The number of curves increases rapidly at increasing of waveguide radius. It is interesting to note that all dispersion branches of the dense bunch are within the frequency band of 2-2.5 GHz. Apparently the dense bunch of dispersion characteristics related to plasma f_{mpzz} and f_{epzz} frequencies. The cutoff frequencies of all dispersion characteristics of the dense bunch are the same and equal to f~2.46 GHz. The dispersion curves fan out from a point with a value equal to f_{mpxx}.

Second dense bunch of dispersion curves is at the electric plasma frequency f_{epxx}~3.46 GHz. The number of curves increases rapidly at increasing of waveguide radius. All dispersion characteristics are within the frequency band of 2.5 GHz and 3.46 GHz.

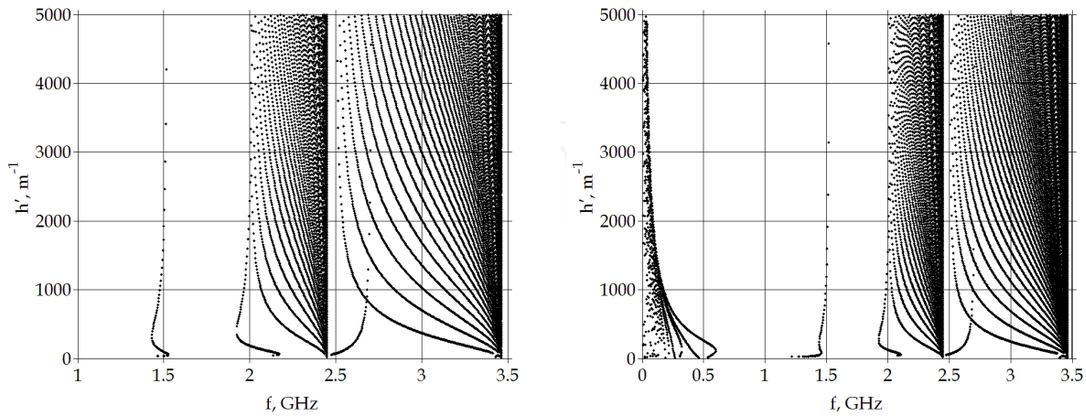

Fig. 5.5. The phase constant dependencies of propagating eigenmodes on the open plasmonic metamaterial waveguide with (a) r=10 mm (b) r=15 mm.

The dispersion characteristics on the right side of the bunch are more vertical. The greatest number of modes can be excited at the electric plasma frequency f_{epxx}~3.46 GHz in the comparison with other plasma frequencies. The cutoff frequencies of dispersion characteristics of this dense bunch are the same and equal to f~3.46 GHz. We did not find the plasmonic metamaterial waveguide eigenmodes in the frequency range from 3.5 GHz till 2000 GHz.

We expanded the searching of eigenmodes on frequencies below f=1 GHz for the plasmonic waveguide with r= 15 mm. In Fig. 5.5 (b) is shown eigenmodes dispersion characteristics of plasmonic metamaterial waveguide in the frequency range from 5 MHz till 3.5 GHz. We present here more detailed calculations of the dispersion characteristics of the plasmonic waveguide eigenmodes with the radius equal to 15 mm (Figs. 5.6 and 5.7). Here are presented the new dispersion characteristic branches of waveguide eigenmodes in the band of frequency from 5 MHz till 600 MHz (Fig. 5.6 (a)). We see that the dispersion curves have the clear expressed cutoff frequencies and they have an opposite slope in the comparison with dispersion curves of open ordinary waveguides (Nickelson et al., 2011; Asmontas et al., 2010).

It should be stressed that these very low frequency dispersion characteristics have obtained by solving of Maxwell's equations with certain boundary conditions. These low frequency modes are also the metamaterial waveguide eigenmodes.

In the Fig. 5.6 (b) is shown the dispersion characteristic of a singular mode on a larger scale. We see that this mode from 1.35 till ~1.45 GHz is a static mode, because no dependence on the frequency. We can observe the anomaly dispersion closed to f~ 1.45 GHz and the very strong dispersion in the frequency band over ~1.47 GHz. We can see the dispersion curves in the area of cutoff frequencies on a larger scale 1.9-2.5 GHz in Figs 5.7(a) and (b). We can note the anomalous dispersion hook of eigenmodes in the band f=1.9-2 GHz.

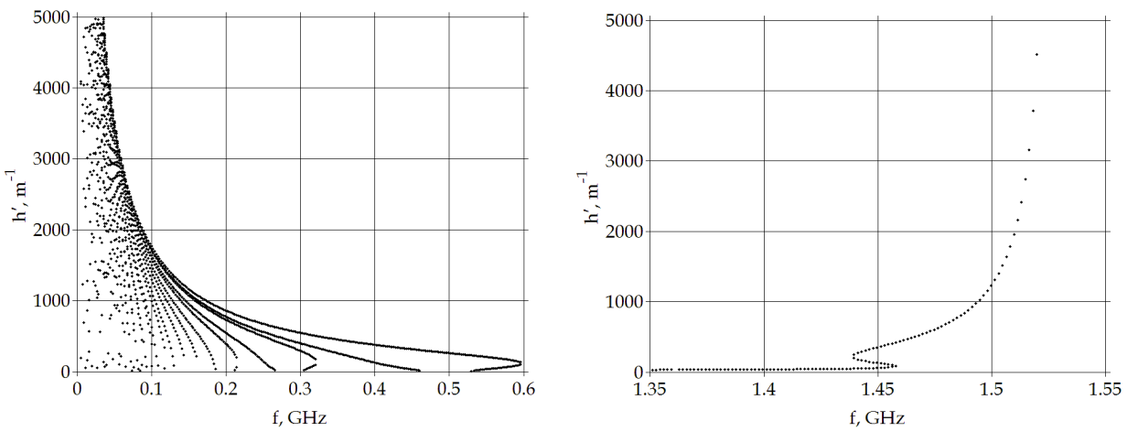

(a) (b)

Fig. 5.6. Low frequency branches of phase constants of open plasmonic metamaterial waveguide with r=15 mm at frequencies: (a) f=0.005-0.06 GHz and (b) f=1.35-1.55 GHz.

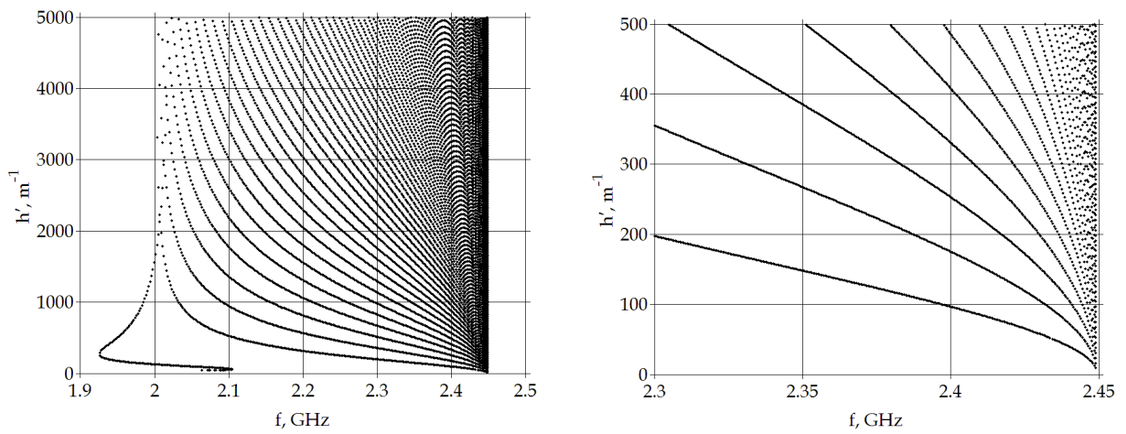

(a) (b)

Fig. 5.7. Frequency branches of phase constants of waveguide with r=15 mm at frequencies: (a) 1.9-2.5 GHz and (b) 2.3-2.45 GHz.

6. Conclusions

1. The open anisotropic metamaterial waveguides with seven different radii were investigated by using of our computer programs that have written in MATLAB language. The algorithm is based on the partial area method.
2. We discovered the anomalous dispersion of the analyzed plasmonic waveguide eigenmodes (Figs. 3.2-3.5).
3. We find a mode with the cutoff frequency close to f=1.5 GHz with some anomalous features, e.g. the small changes in the frequency produce the very large changes in phase. This property could be useful in practical realizations.

7. Microwave scattering and absorption by layered metamaterial-glass cylinders

In this section we are going to give our calculation results for a single-layered cylinder and a twelve layered cylinder. The single–layered cylinder consists of a metamaterial core which is coated with an acrylic-glass layer. The twelve-layered cylinder consists of a conductor core which is covered with 12 metamaterial and acrylic-glass alternately layers. The acrylic-glass material is an external layer of each cylinder. The calculation of the scattered (reflected) and absorbed powers are based on the rigorous solution of scattering boundary problem (Nickelson & Bucinskas, 2011). The solution of mentioned electrodynamical problems and expressions of absorbed and scattered powers are given in article (Bucinskas et al., 2010).

The number and thickness of layers is not limited in the presented algorithm. The central core of multilayered cylinder can be made of different isotropic materials as a metamaterial, a ceramic matter or a semiconductor as well as of a perfect conductor. The isotropic coated layers can be of strongly lossy (absorbed) materials.

The signs of the complex permittivity and the complex permeability can be negative or positive in different combinations.

Here are presented the scattered and absorbed power of layered cylinder dependent on the hypothetic metamaterial permittivity and permeability signs and losses. We used for calculations our computer programs which are written in FORTRAN language.

The extern radius of both (single- and twelve-layered) cylinders is the same and equal to 2 mm. We show here our results only in the frequency range from 1 till 120 GHz. We present dependencies of the scattered and absorbed powers by the cylinders at the incident perpendicularly (the angle $\psi = 0^o$, Fig. 7.1) and parallel (the angle $\psi = 90^o$, Fig. 7.1) polarized microwaves. An incident angle of microwave is $\theta = 90^o$ here.

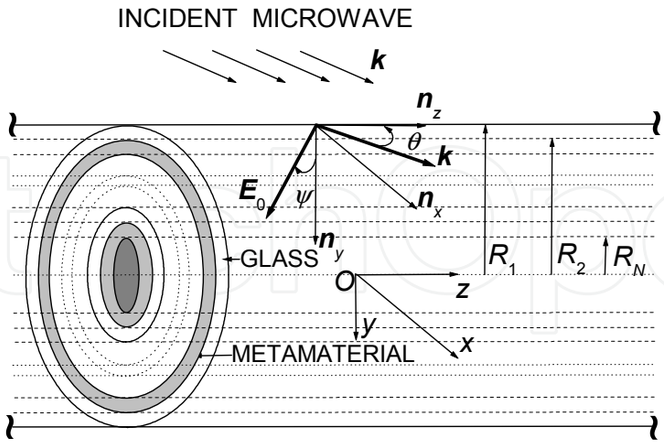

Fig. 7.1. *N*-layered metamaterial-glass cylinder model and designations

We admitted that acrylic-glass material is a non-dispersive and weakly lossy one with the complex permittivity $\varepsilon_g = \varepsilon_g' - i\varepsilon_g'' = |\varepsilon_g| \exp(-i\,\delta_g) = 3.8 - i\,0.0005$, i.e. the phase of the complex glass permittivity is $\delta_g = \arctan(\varepsilon_g'/\varepsilon_g'') = 1.3 \cdot 10^{-4}$ [rad] and the glass permeability is equal to $\mu_g = 1$.

The complex metamaterial permittivity is $\varepsilon_{met} = \varepsilon'_{met} - i\varepsilon''_{met} = |\varepsilon_{met}| \exp(-i\,\delta_{met})$. The complex permeability is $\mu_{met} = \mu'_{met} - i\mu''_{met} = |\varepsilon_{met}| \exp(-i\,\delta_{met})$. The metamaterial ε_{met} and μ_{met} are the same for the single-layer and twelve-layer cylinders. The module of the metamaterial permittivity is $|\varepsilon_{met}|=20$ and the metamaterial permeability is $|\mu_{met}|=2$. The phase of metamaterial permittivity is $\delta_{\varepsilon,met}=0.7854$ [rad] and the phase of permeability is $\delta_{\mu,met}=0.6981$ [rad] for the single-layer and twelve layer cylinders.

We present here the absorbed power by the acrylic-glass layer (Fig. 7.3) and the absorbed power by the metamaterial (Fig. 7.4) for the single-layer cylinder. The total absorbed power by single-layered cylinder is equal to the sum of absorbed powers by metamaterial and acrylic-glass. And we show here the total absorbed power by all layers of the twelve-layered cylinder.

In Figs 7.2-7.6 are presented the averaged scattered or absorbed power values per oscillation period for the unit length of the metamaterial-glass cylinder.

The absorbed and scattered power calculations were fulfilled using by formula (28) in (Bucinskas et al., 2010)]. The integral of the formula has a positive sign when we calculate the scattered power. And this integral has a negative sign when we calculate the absorbed power. For this reason the scattered power has a positive value and the absorbed power has a negative one (see Figs 7.2-7.6).

We presented here the dependencies of scattered and absorbed powers of the single-layered cylinder on signs of ε'_{met}, ε''_{met}, μ'_{met} and μ''_{met}, i.e. when metamaterial is double positive (DP), ε- single negative (SN) or μ - single negative (SN), double negative (DN).

7.1 Numerical analysis of the scattered and absorbed microwave power of the single-layer cylinder

In this subsection we investigate the scattered and absorbed powers of the incident microwave by the cylinder consists a core of metamaterial which is covered with a single-layer of acrylic-glass. The external cylinder radius is $R_1=2$ mm and the cylinder core has radius $R_2=1.8$ mm, so the thickness of the glass layer is 0.2 mm.

Nowadays there is a huge interest to the composite materials with untraditional values of the complex permittivity ε_{met} and the complex permeability μ_{met}. We analyzed here the scattered and absorbed powers for four versions of hypothetic metamaterial parameter signs. The complex metamaterial permittivity $\varepsilon_{met}=s_1|\varepsilon_{met}|\exp(-s_2 i\delta_{met,\varepsilon})$ was taken for two combinations of signs, when $s_1=s_2=\pm1$. It is known that each metamaterial is intended for use in a specific frequency range and has a specific value of the effective permittivity and permeability at the certain frequency. For this reason we took the absolute values of real and imaginary parts of permittivity ε_{met} and permeability μ_{met} constant at all frequencies in our calculations. And the major impact makes the sizes' relation of wavelength and cylinder layers.

In figures 7.2-7.4 of this section are analyzed how the signs of the complex metamaterial permittivity and permeability influence on the scattered and absorbed powers when the plane perpendicularly or parallel polarized microwave impinges on the metamaterial-glass cylinder (Fig. 7.1).

Designations in Figs 7.2-7.4 correspond: the curve 1 is for a DP material when $s_1=s_2=s_3=s_4=+1$ (line with black squares); the curve 2 is for a SN material when $s_1=s_2=+1$, $s_3=s_4=-1$ (line with empty squares); the curve 3 is for a SN material when $s_1=s_2=-1$, $s_3=s_4=+1$ (line with black triangulars); the curve 4 is for a DN material when $s_1=s_2=s_3=s_4=-1$ (line with empty triangulars).

The scattered and absorbed dependences of the metamaterial-glass cylinder when the incident microwave has the perpendicular or parallel polarization are shown in Figs 7.2-7.4. In Fig. 7.2 is presented the dependence of total scattered power W^S on the microwave frequency *f* at two polarizations. We see that the character of curves for all metamaterial sign versions (curves 1-4) is the same at the perpendicular polarization. A comparison of curves 1-4 (Fig. 7.2(a)) shows that only curve 3 that describes by the metamaterial permittivity and permeability signs $s_1=s_2=-1$, $s_3=s_4=+1$ is the most different in comparison with other three cases. At the beginning the scattered power grows till the maximum value after that decreases till the minimum and later increases again with increasing of frequency. The total scattered power maximums of all curves are in the frequency range about 44-53 GHz. Curves 1 and 4 practically coincide with each other. The lowest scattered power is for the curve 3 at the frequencies about 1-35 GHz and the total scattered power minimum exists for the curve 2 approximately at the frequency 80 GHz.

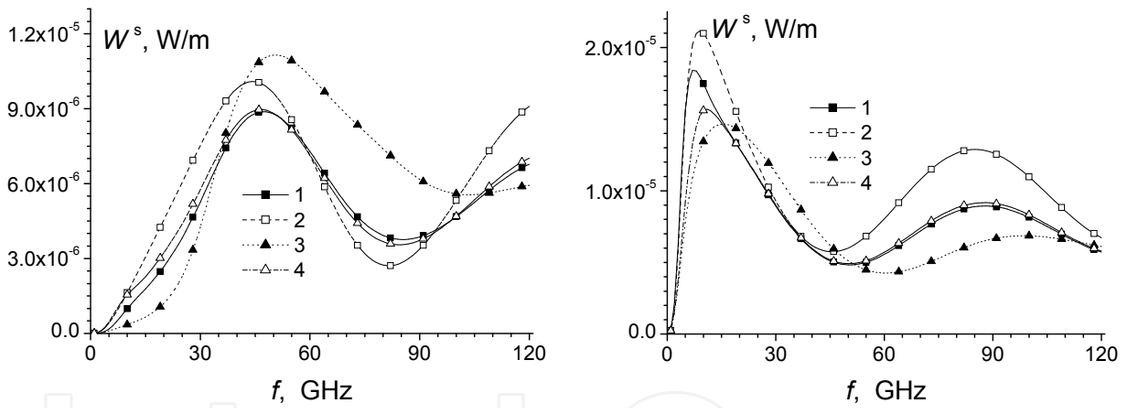

(a) (b)

Fig. 7.2. Scattered power of metamaterial-glass cylinder on the frequency of incident (a) - perpendicular and (b) - parallel polarized microwaves.

The total scattered power of the incident perpendicularly and parallel polarized microwaves (Fig. 7.2(a, b)) are different. The scattered microwave power curves for the incident parallel polarized microwave have two maximums in the frequency range 1-120 GHz. The first position of the scattered power maxima are in the narrow frequency interval about 10-15 GHz and the second position of the maxima is in the interval 85-100 GHz. The largest scattering is at the lower frequencies. The maximum scattering is higher for the incident parallel polarized microwave in comparison with the incident perpendicularly polarized one. While the total scattered power curves for the incident perpendicularly polarized microwave (Fig. 7.2(a)) have only one maximum.

In Fig. 7.3 is presented the absorbed microwave power $W^{a,glass}$ by the coated glass layer at two microwave polarizations. We see that the behavior of the microwave power absorption strongly depends on the signs s_1, s_2, s_3, s_4 of the permittivity and the permeability. The absorption is especially different at the higher frequencies. We see that the absorption power of the glass layer is larger at higher frequencies.

In Fig. 7.3(b) is presented the absorbed power by the coated glass layer for the incident parallel polarized microwave. There are some small distortion "hooks" of the absorbed power at the low frequencies. The absorbed power by glass layer increases with increasing of frequencies (curves 1, 3, 4) for frequencies that are larger than 20 GHz. The absorbed power is approximately constant when the SN metamaterial core permittivity and permeability have signs $s_1=s_2=+1$, $s_3=s_4=-1$.

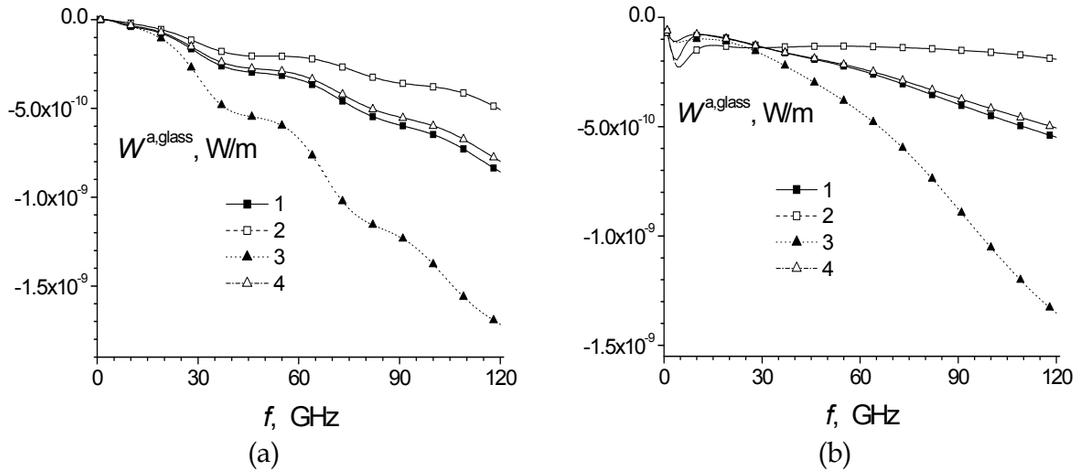

Fig. 7.3. Absorbed power by the acrylic-glass layer on the frequency of incident (a) - perpendicular and (b) - parallel polarized microwaves.

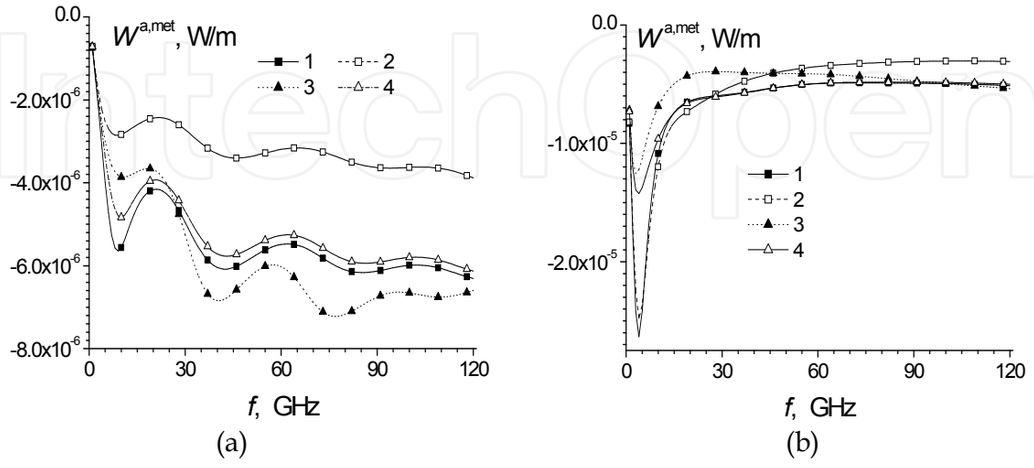

Fig. 7.4. Absorbed power by metamaterial core on the frequency of incident (a) - perpendicular and (b) - parallel polarized microwaves

In Fig. 7.4(a) is given the absorbed power by the metamaterial core of the cylinder for the perpendicular microwave polarization. We see that the $W^{a,met}$ magnitudes have the pronounced wave-like nature dependent on the frequency. The metamaterial core absorption has the largest absolute value when the metamaterial permittivity has some negative values and the permeability has some positive values (curve 3). In Fig. 7.4(b) is given the metamaterial core absorbed power $W^{a,met}$ for the incident parallel polarized microwave. We see that the absorbed-powers have maximum values at about 5 GHz and their values vary slightly after 20 GHz with increasing of frequency. The absorption by the metamaterial is the largest at the low frequencies (curves 1 and 2) when the metamaterial has the positive permittivity. The comparison of absorbed powers in figures 7.3 and 7.4 shows that dependencies are absolutely different.

7.2 Numerical analysis of the scattered and absorbed microwave power of twelve-layer cylinder

In this subsection we present the total scattered power and the total absorbed power of incident microwave by the cylinder that consists of conductor core covered with 12 metamaterial and glass alternately layers. Designations in Figs 7.5 and 7.6 correspond: the curve 1 is for a DP material when $s_1=s_2=s_3= s_4=+1$ (line with black squares) and the curve 2 is for a DN material when $s_1=s_2=s_3= s_4=-1$ (line with empty triangulars).

In Figs 7.5 and 7.6 the permittivities and permeabilities metamaterial and acrylic-glass are the same as in the previous subsection. We see that the total scattered and absorbed powers strongly dependent on the polarization of incident wave. The characteristics of perpendicular polarized wave (Figs 7.5(a) and 7.6(a)) and the parallel polarized wave (Figs 7.5(b) and 7.6(b)) are completely different. Particularly noticeable the correlation between the total scattered and absorbed powers for the parallel polarized wave of the twelve-layered cylinder. We see that extremums of the total scattered and absorbed powers coincide in the frequency scale. For example, when the scattered power of cylinder has a maximum (Fig. 7.5(b)) then the absorbed power has a minimum (Fig. 7.6(b)) at f~10 GHz.

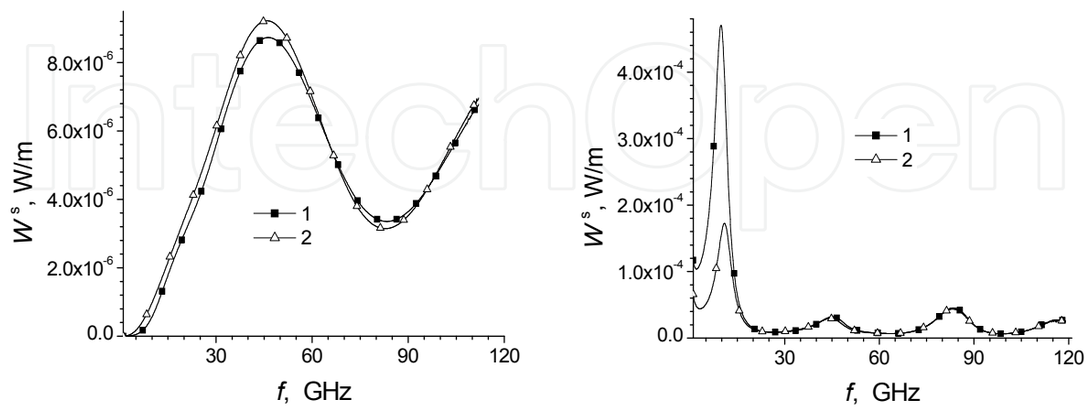

(a) (b)

Fig. 7.5. Total scattered power of twelve layer metamaterial-glass cylinder on the frequency of incident (a) - perpendicular and (b) - parallel polarized microwaves

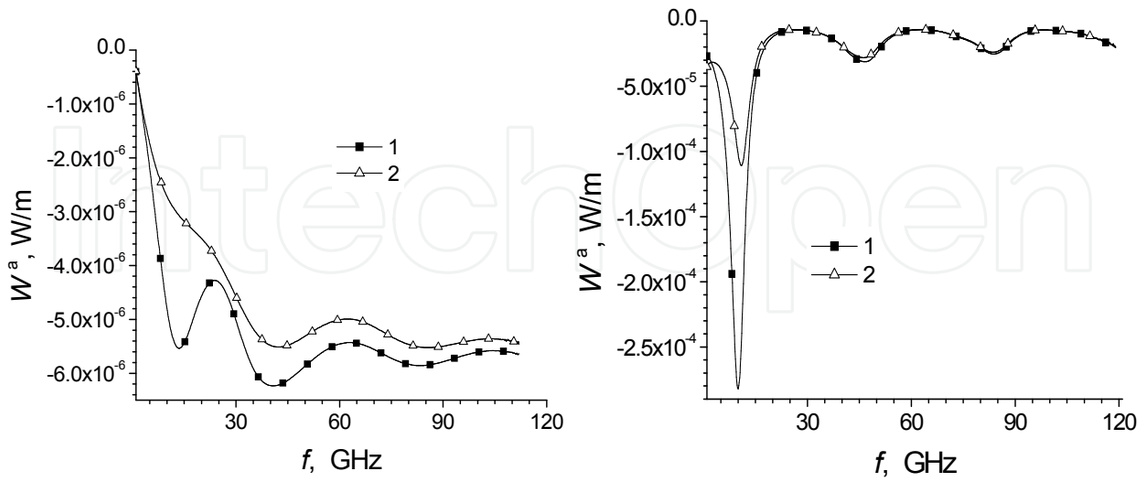

Fig. 7.6. Total absorbed power by the twelve layered metamaterial-glass cylinder on the frequency of incident (a) - perpendicular and (b) - parallel polarized microwaves.

The comparison of scattered power of single- and twelve-layered cylinders shows that dependencies for the perpendicular polarized microwave are very similar. The scattering power maximum is at ~45 GHz and the minimum is at ~80 GHz (Figs 7.2(a) and 7.5(a)).

The scattered powers of single- and twelve-layered cylinders for the parallel polarized microwave are different (Figs 7.2(b) and 7.5(b)). We see that the scattered power of single-layered cylinder has only two maximums in the considered frequency range while the twelve-layered cylinder dependency has four maximums. The first scattered power maximum of twelve-layered cylinder has a sharp pike and is more than twice larger in comparison with the single-layered cylinder (Figs 7.2(b) and 7.5(b)).

Comparing Figs 7.3(a), 7.4(a) and 7.6(a) for perpendicular polarized microwave we see that the absorbed power determined mainly due to metamaterial losses. The absorbed power extremums of the twelve layered cylinder (Fig. 7.6 (a)) shifted to the higher frequencies in the comparison with single-layered cylinder (Fig. 7.4(a)) for the DP metamaterial (curve 2).

Comparing curves for single- and twelve–layered cylinders (Fig. 7.4(a), curve 4 and Fig. 7.6 (a), curve 2) when the metamaterial is SN we can note that their lineaments are different at the low frequencies.

The dependencies of absorbed parallel polarized microwave power for single-layered and twelve-layered cylinders in general are alike. The first minimum of absorbed power is shifted from ~5 GHz (Fig. 7.4(b)) till 10 GHz (Fig. 7.6 (b)) i.e. with growing of the number of layers the minimum shifted to the side of higher frequencies. The absorbed power dependency of twelve layered cylinder has a wavy behavior in the frequency range from 20 GHz till 120 GHz in a comparison with the single-layered one.

8. Conclusions

1. We found that the scattered power dependences have wave behaviors. The minimal scattering from the metamaterial-glass cylinder are observed for the every metamaterial with some sign combinations of the permittivity and the permeability at the special frequency range (Figs 7.2).
2. We found that the largest absorbed power by the coated acrylic-glass layer is observed for the case when the metamaterial is a single negative material with the negative permittivity. The absorbed power of the glass layer increases with increasing of frequency in the range 1-120 GHz for both microwave polarizations (Figs 7.2).
3. The metamaterial core absorbed power of the parallel polarized incident microwave has the minimum value at low frequencies and slightly dependent on the frequency at the range 20-120 GHz (Fig. 7.4(b)).
4. The comparison of single- and twelve- layered cylinder characteristics shows that the absorbed power extremums shift to the direction of higher frequencies when the number of layers becomes larger (Figs 7.4 and 7.6).

9. References

Abdalla, M. A.& Hu, Z. (2009). Multi-band functional tunable lh impedance transformer, *J. of Electromagn. Waves and Appl.,* Vol. 23, pp. 39–47, ISSN 0920–5071.

Asmontas, S.; Nickelson, L.; Bubnelis, A.; Martavicius, R. & Skudutis, J. (2010). Hybrid Mode Dispersion Characteristic Dependencies of Cylindrical Dipolar Glass Waveguides on Temperatures, *Electronics and Electrical Engineering*, Vol. 106, No. 10, pp. 83-86, ISSN 1392-1215.

Asmontas, S.; Nickelson, L.; Gric, T. & Galwas, B. A. (2009). Solution of Maxwell's Equations by the Partial Area Method for the Electrodynamical Analyses of Open Lossy Metamaterial Waveguides, *in Proceedings of the International Conference Differential Equations and their Applicat*ions. *DETA–2009,* pp. 17–20, ISBN 978-9955-25-747-9, Panevezys, Lithuania, 10-12 Sept. 2009, TECHNOLOGIJA, Kaunas University of Technology, Kaunas.

Asmontas, S.; Nickelson, L. & Plonis, D. (2009). Dependences of propagation constants of cylindrical n-Si rod on the material specific resistivity, *Electronics and Electrical Engineering,* Vol. 94, No. 6, pp. 57-60, ISSN 1392-1215.

Bai, J.; Shi, S. & Prather, D. W. (2010). Analysis of epsilon-near-zero metamaterial super-tunneling using cascaded ultra-narrow waveguide channels. *Progress In Electromagnetics Research M,* Vol. 14, pp. 113-121, E-ISSN 1559-8985.

Bucinskas, J.; Nickelson, L. & Sugurovas, V. (2010). Microwave scattering and absorption by a multilayered lossy metamaterial-glass cylinder, *Progress In Electromagnetics Research,* PIER105, pp. 103–118, ISSN 1070-4698, E-ISSN 1559-8985.

Bucinskas, J.; Nickelson, L. & Sugurovas, V. (2010). Microwave diffraction characteristic analysis of 2D multilayered uniaxial anisotropic cylinder, *Progress In Electromagnetics Research*, PIER109, pp. 175-190, ISSN 1070-4698, E-ISSN 1559-8985.

Chen, H.; Wu, B.-I. & Kong, J. A. (2006) Review of electromagnetic theory in left-handed materials *J. of Electromagn. Waves and Appl.,* Vol. 20, No. 15, pp. 2137–2151, ISSN 0920–5071.

Engheta, N. & Ziolkowski R.W. (2005). A positive future for double-negative metamaterials. *IEEE Transactions on microwave theory and techniques,* Vol. 53, No. 4, pp. 1535- 1556, ISSN 0018–9480.

Feng, T. H.; Li, Y.H.; Jiang, H. T.; Li W. X., Yang F.; Dong X. P.& Chen H. (2011) Tunable single-negative metamaterials based on microstrip transmission line with varactor diodes loading, *Progress In Electromagnetics Research,* PIER 120, 35-50, ISSN 1070-4698, E-ISSN 1559-8985.

Gric, T. & Nickelson, L. 2011. Electrodynamical investigation of the photonic waveguide structure. *Electronics and Electrical Engineering*, Vol. 111, No. 5, pp. 1-4, ISSN 1392-1215.

Gric, T.; Nickelson, L. & Asmontas, S. (2010). Electrodynamical characteristic particularity of open metamaterial square and circular waveguides. *Progress In Electromagnetics Research,* PIER109, pp. 361-379, ISSN 1070-4698, E-ISSN 1559-8985.

Gric, T.; Ašmontas, S. & Nickelson, L. (2010). 3D vector electric field distributions and dispersion characteristics of open rectangular and circular metamaterial waveguides, *Proceedings of 4th Microwave & Radar Week: 18th Int. Conf. on Microwaves, Radar, and Wireless Communicatins MIKON-2010,* Vol. 2, pp. 578–581, ISBN 978-9955-690-20-7, IEEE Catalog Number CFP10784-PRT, Vilnius, Lithuania, 14-16 June 2010, JUSIDA, Vilnius.

Ko, S.-T. & Lee, J.-H. (2010). Dual Property of Mu-near-zero to Epsilon-near-zero material, *J.of the Korean Physical Society*, Vol. 57, No. 1, pp. 51-54, ISSN 03744884.

Kong, J.A. (2008). *Electromagnetic wave theory,* 1016 p., EMW Publishing, ISBN 0-9668143-9-8, Cambridge, Massachusetts, USA.

Li, M.-H.; Yang, H.-L.; Hou, X.-W.; Tian, Y.& Hou, D.-Y. (2011). Perfect metamaterial absorber with dual bands, *Progress In Electromagnetics Research,* PIER108, 37-49, ISSN 1070-4698, E-ISSN 1559-8985.

Liu, S.-H.; Liang, C.-H.; Ding, W.; Chen, L. & Pan, W.-T. (2007). Electromagnetic wave propagation through a slab waveguide of uniaxially anisotropic dispersive metamaterial, *Progress In Electromagnetics Research*, PIER76, pp. 467–475, ISSN 1070-4698, E-ISSN 1559-8985.

Lopez-Garcia, B.; Murthy, D. V. B. & Corona-Chavez, A. (2011). Half mode microwave filters based on epsilon near zero and mu near zero concepts. *Progress In Electromagnetics Research,* Vol. 113, pp. 379-393, ISSN 1070-4698, E-ISSN 1559-8985.

Luo, J.; Chen, H.; Lai, Y.; Xu, P. & Gao L. (2011) Anomalous transmission properties of epsilon-near-zero metamaterials. *Proceedings of* Progress In Electromagnetics Research Symposium, pp. 1299-1302, ISSN 1559-9450, ISBN 978-1-934142-18-9, Suzhou, China, 12-16 Sept. 2011, The Electromagnetics Academy, Cambridge, MA 02138.

Liu, R.; Cheng, Q.; Hand, T.; Mock J.J.; Cui T. J.; Cummer S. A. &Smit, D. R.(2008) Experimental Demonstration of Electromagnetic Tunneling Through an Epsilon-Near-Zero Metamaterial at Microwave Frequencies, Physical Review Letters, PRL 100, pp. 023903-(1-4), ISSN 0031-9007.

Mirza, O.; Sabas, J. N.; Shi, S. & Prather, D. W. (2009) Experimental demonstration of metamaterialbased phase modulation, *Progress In Electromagnetics Research,* PIER 93, pp. 1–12, ISSN 1070-4698, E-ISSN 1559-8985.

Mirzavand, R.; Honarbakhsh, B.; Abdipour, A. & Tavakoli A. (2009). Metamaterial-based phase shifters for ultra wide-band applications. *J. of Electromagn. Waves and Appl.,* Vol. 23, pp. 1489–1496, ISSN 0920–5071.

Nickelson, L.& Bucinskas, J. (2011). Microwave diffraction dependencies of a conductor cylinder coated with twelve glass and semiconductor layers on the *n*-Si specific resistivity. *Electronics and Electrical Engineering,* Vol. 115, No. 9, pp. 47-50, ISSN 1392-1215.

Nickelson, L.; Gric, T. & Asmontas, S. (2011). Chapter 6: Electrodynamical modelling of open cylindrical and rectangular carbide waveguides, In: *Properties and applications of Silicon Carbide*, (Ed. Rosario Gerhardt), 535 p., pp 115-141, InTech, ISBN 978-953-307-201-2, Rijeka, Croatia.

Nickelson, L.; Bubnelis, A.; Baskys, A. & Navickas, R. (2011). The magnetoactive *p*-Ge rod waveguide loss analysis on the concentration of two component hole charge carriers, *Electronics and Electrical Engineering,* Vol. 110, No. 4, pp. 53-56, ISSN 1392-1215.

Nickelson, L.; Asmontas, S.; Malisauskas, V. & Martavicius, R. (2009). The dependence of open cylindrical magnetoactive *p*-Ge and *p*-Si plasma waveguide mode cutoff frequencies on hole concentrations, *Journal of Plasma Physics,* Vol. 75, No. 1, pp. 35–51, ISSN 0022-3778.

Nickelson, L.; Gric, T.; Asmontas, S. & Martavicius, R. (2009) Analyses of the gyroelectric plasma rod waveguide, *Proceedings of 17th IEEE International Pulsed Power Conference*, pp. 727-730, IEEE Catalog Number: CFP09PPC-DVD, Library of Congress: 2009901215, DC USA, ISBN 978-1-4244-4065-8, Washington, DC, USA**,** 29 June – 2 July 2009.

Nickelson, L.; Gric, T.; Asmontas, S. & Martavicius, R. (2008). Electrodynamical analyses of dielectric and metamaterial hollow-core cylindrical waveguides. *Electronics and Electrical Engineering*, Vol. 82, No. 2, pp. 3-8, ISSN 1392-1215.

Nickelson, L.; Galwas, B.A.; Gric, T. & Ašmontas, S. (2008). Electric field distributions in the cross sections of the metamaterial hollow-core and rod waveguides, *Proceedings of 17th International Conference on Microwaves, Radar and Wireless Communication MIKON-2008,* Vol. 2, pp. 497-500, ISBN 978-1424-431-22-9, Wrocław, Poland, 19-21 May 2008, MDruk, Warszawa, Poland.

Nickelson, L. & Shugurov, V. (2005). *Singular integral equations' method for the analysis of microwave structures*, 348 p., VSP Brill Academic Publishers, ISBN 90-6764-410-2, Leiden-Boston, The Netherlands.

Oraizi, H. & Abdolali, A. (2009) Some aspects of radio wave propagation in double zero metamaterials having the real parts of epsilon and mu equal to zero, *J. of Electromagn. Waves and Appl.*, Vol. 23, pp. 1957–1968, ISSN 0920–5071.

Penciu, R.S.; Kafesaki, M.; Gundogdu, T.F.; Economou, E.N. & Soukoulis, C.M. (2006). Theoretical study of left-handed behavior of composite metamaterials. *Photonics and Nanostructures – Fundamentals and Applications*, Vol. 4, pp. 12-16, ISSN 1569-4410.

Wang, B. &. Huang, K.-M (2010). Shaping the radiation pattern with mu and epsilon-near-zero metamaterials. *Progress In Electromagnetics Research,* PIER 106, pp. 107-119, ISSN 1070-4698, E-ISSN 1559-8985.

Zhou, H.; Ding, F.; Jin, Y. & He, S. L. (2011). Terahertz metamaterial modulators based on absorption, *Progress In Electromagnetics Research,* PIER119, pp. 449-460, ISSN 1070-4698, E-ISSN 1559-8985.

Zhou, H.; Pei,Z.; Qu, S.; Zhang, S. & Wang, J. (2009) A planar zero-index metamaterial for directive emission, *J. of Electromagn. Waves and Appl.,* Vol. 23, pp. 953–962, ISSN 0920–5071.

Zhu, B.; Wang, Z.; Huang, C.; Feng, Y.; Zhao, J. & Jiang, T. (2010) Polarization insensitive metamaterial absorber with wide incident angle, *Progress In Electromagnetics,* PIER101, pp. 231-239, ISSN 1070-4698, E-ISSN 1559-8985.

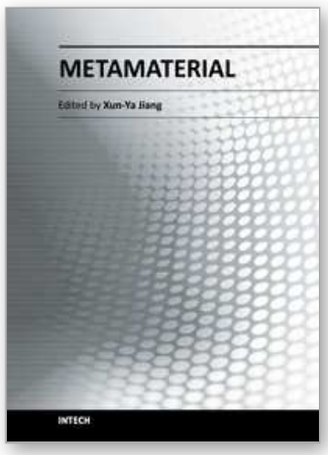

Metamaterial

Edited by Dr. Xun-Ya Jiang

ISBN 978-953-51-0591-6
Hard cover, 620 pages
Publisher InTech
Published online 16, May, 2012
Published in print edition May, 2012

In-depth analysis of the theory, properties and description of the most potential technological applications of metamaterials for the realization of novel devices such as subwavelength lenses, invisibility cloaks, dipole and reflector antennas, high frequency telecommunications, new designs of bandpass filters, absorbers and concentrators of EM waves etc. In order to create a new devices it is necessary to know the main electrodynamical characteristics of metamaterial structures on the basis of which the device is supposed to be created. The electromagnetic wave scattering surfaces built with metamaterials are primarily based on the ability of metamaterials to control the surrounded electromagnetic fields by varying their permeability and permittivity characteristics. The book covers some solutions for microwave wavelength scales as well as exploitation of nanoscale EM wavelength such as visible specter using recent advances of nanotechnology, for instance in the field of nanowires, nanopolymers, carbon nanotubes and graphene. Metamaterial is suitable for scholars from extremely large scientific domain and therefore given to engineers, scientists, graduates and other interested professionals from photonics to nanoscience and from material science to antenna engineering as a comprehensive reference on this artificial materials of tomorrow.

How to reference

In order to correctly reference this scholarly work, feel free to copy and paste the following:

L. Nickelson, S. Asmontas, T. Gric, J. Bucinskas and A. Bubnelis (2012). Electrodynamical Analysis of Open Lossy Metamaterial Waveguide and Scattering Structures, Metamaterial, Dr. Xun-Ya Jiang (Ed.), ISBN: 978-953-51-0591-6, InTech, Available from: http://www.intechopen.com/books/metamaterial/electrodynamical-analysis-of-open-lossy-metamaterial-waveguide-and-scattering-structures

INTECH
open science | open minds

InTech Europe
University Campus STeP Ri
Slavka Krautzeka 83/A
51000 Rijeka, Croatia
Phone: +385 (51) 770 447
Fax: +385 (51) 686 166
www.intechopen.com

InTech China
Unit 405, Office Block, Hotel Equatorial Shanghai
No.65, Yan An Road (West), Shanghai, 200040, China
中国上海市延安西路65号上海国际贵都大饭店办公楼405单元
Phone: +86-21-62489820
Fax: +86-21-62489821

IntechOpen